Lithos 320–321 (2018) 302–314

Contents lists available at ScienceDirect

Lithos

journal homepage: www.elsevier.com/locate/lithos

A red-corundum-bearing vein in the Rai–Iz ultramafic rocks, Polar Urals, Russia: the product of fluid activity in a subduction zone

Fancong Meng [a,*], Vladimir R. Shmelev [b], Ksenia V. Kulikova [c], Yufeng Ren [a]

[a] Institute of Geology, Chinese Academy of Geological Sciences (CAGS), Beijing 100037, China
[b] Institute of Geology and Geochemistry, Uralian Division, RAS, Ekaterinburg 620075, Russia
[c] Institute of Geology, Komi Science Center of Uralian Division, RAS, Syktyvkar 167982, Russia

ARTICLE INFO

Article history:
Received 26 April 2018
Accepted 20 September 2018
Available online 28 September 2018

Keywords:
Red corundum
Phlogopite
Zircon
Fluid
Rai–Iz ultramafic rocks
Polar Urals

ABSTRACT

The veins in the mantle wedge peridotite can record the activity of slab-derived melt/fluid, which is the reflection of the material circulation between crust and mantle. A red-corundum-bearing vein is present in the Rai–Iz ultramafic rocks in the Polar Urals, Russia. The ultramafic rocks are harzburgite and dunite, and the red corundum-bearing rocks consist of phlogopite, paragonite, oligoclase, red corundum, and chromian spinel. Red corundum occurs as prophyroblasts or fine grains that contain 92–98 wt% Al_2O_3 and 2–7 wt% Cr_2O_3. Chromian spinel has Cr# values ([100Cr/ (Cr + Al)] atomic ratio) of 46–78. Oligoclase is characterized by An values of 20–30. Phlogopite is Ba-rich (BaO = 0.8–2.7 wt%) and paragonite is Sr-rich (SrO = 0.8–2.3 wt%). Zircons from the oligoclasite show oscillatory zoning and Th/U values of <0.2, indicating crystallization from fluid. A zircon weighted-mean $^{206}Pb/^{238}U$ age of 382 ± 2 Ma and a phlogopite $^{40}Ar/^{39}Ar$ plateau age of 377 ± 3 Ma indicate that the red-corundum-bearing vein formed at 380 Ma. The occurrence and formation age of the vein, structure and composition of vein minerals, and zircon εHf values (−11 to +13) suggest that the vein was the product of interaction between a subduction-zone-derived fluid and mantle wedge peridotite.

1. Introduction

Corundum rarely occurs in feldspathic rocks in ultramafic rocks and in ultramafic rocks that are poor in Al_2O_3 and SiO_2. However, it has been identified in garnet peridotite and pyroxenite, including in ultrahigh-pressure garnet peridotite in the Donghai area, Sulu Terrane, eastern China (Zhang et al., 2004), garnet pyroxenite from the Maowu area, Dabieshan, central China (Okay, 1994), and garnet peridotite from the northern Dominican Republic (Hattori et al., 2010). These corundum-bearing rocks are considered to have formed by metamorphism, with Al- or plagioclase-rich cumulate protoliths (Hattori et al., 2010; Okay, 1994; Zhang et al., 2004). Corundum also occurs in veins and lenses that cut serpentinite or peridotite. Corundum-bearing veins or lenses have been identified in serpentinite in the Umba River area, NE Tanganyika (Solesbury, 1967), in the Buck Creek peridotites from North Carolina and Georgia, USA (Hadley, 1949; Pratt, 1906), in peridotites near Spanish Peak, California, USA (Lawson, 1904), and in the Berezovskyi corundum deposit in the South Urals, Russia (Kolesnik, 1976), in addition to red-corundum-bearing veins in the Rai–Iz ultramafic rocks (Bryanchaninova et al., 2004; Ishimaru et al., 2015). The origin of this type of corundum is debated, and the following processes have been proposed: (1) crystallization of magma (Lawson, 1904; Pratt, 1906); (2) metasomatism of ultramafic rocks (Kolesnik, 1976); and (3) desilication of pegmatites (Simonet et al., 2008). The minerals of the red-corundum-bearing vein in the Rai–Iz ultramafic rocks have been described in detail by numerous studies (Bryanchaninova et al., 2004; Goldny et al., 2003; Ishimaru et al., 2015). However, these studies proposed two different theories for the genesis of the red corundum mineralization: (1) metasomatism of ultramafic rocks, involving metasomatic fluids derived from ultramafic rocks (Bryanchaninova et al., 2004; Makeyev, 2006), or a subduction zone (Goldny et al., 2003; Ishimaru et al., 2015); and (2) metamorphic differentiation of the ultramafic rocks (Vakhrusheva et al., 2016). In this paper, we present new zircon U—Pb and $^{40}Ar/^{39}Ar$ geochronology data, detailed petrographic observations, and mineral chemistry data. Combined with the results of previous studies, we further constrain the genesis of the corundum-bearing vein in the Rai–Iz peridotite and provide a case for its origin by subduction-fluid metasomatism of mantle wedge peridotite.

2. Geological setting

The Rai–Iz ultramafic massif in the Polar Urals crops out in a crescentic shape protruding northwestwards (Fig. 1a, b), and covers an area of ~380 km^2. Geophysical data reveal that the north and south sections of the massif have thicknesses of 1–1.5 and 4–7 km, and dips of 35°–40°S

* Corresponding author.
E-mail address: mengfancong@yeah.net (F. Meng).

https://doi.org/10.1016/j.lithos.2018.09.025
0024-4937/

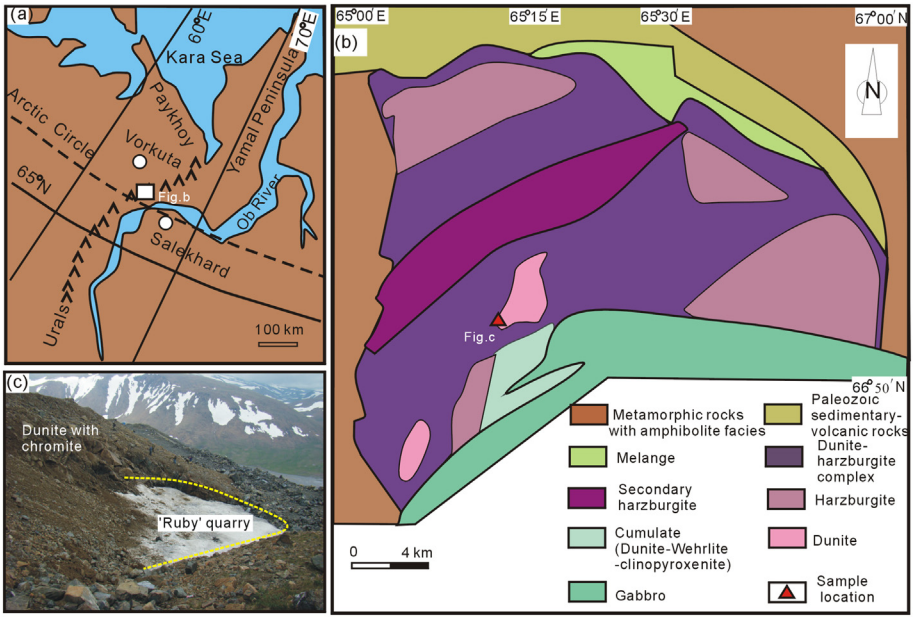

Fig. 1. Geographical position and simplified geological map of the Rai-Iz massif in the Polar Urals (b, modified after Shmelev, 2011); (c) Abandoned querry (covered by snow) for mining red-corundum (ruby)-bearing ore in the Rai –Iz massif.

and 75°–90°S, respectively (Makeyev et al., 1985; Moldavantsev and Kazak, 1977). The cumulate (dunite-websterite-pyroxenite) and gabbro intrusion are exposed to the south, and Paleozoic sedimentary rocks and volcanic–sedimentary rocks that underwent greenschist-facies metamorphism to the north. A mélange comprising schistose serpentinite, glaucophane-bearing amphibolite schist, and rodingite is exposed in the NE of the massif (Kazak et al., 1976; Makeyev et al., 1985; Moldavantsev and Kazak, 1977; Perevozchikov et al., 1990). Metamorphic rocks with amphibolite facies are exposed along the western and eastern margins of the massif (Fig. 1b; Makeyev et al., 1985).

The Rai–Iz massif consists mainly of dunite and harzburgite (Makeyev et al., 1985; Moldavantsev and Kazak, 1977), and dunite is dominant in the southwestern and western areas. The massif is considered to have undergone polyphase metamorphism and deformation (Perevozchikov et al., 1990). The mineral assemblages comprises early olivine + Ca-rich orthopyroxene + chromian spinel to olivine + Ca-bearing orthopyroxene + diopside + chromian spinel to olivine + Ca-poor orthopyroxene + tremolite + chromian spinel. The massif has also experienced varying degrees of serpentinization (Perevozchikov et al., 1990, 2005). The geochemistry of the peridotite indicates that it formed in a supra-subduction environment (Shmelev, 2011). Chromitite in dunite yielded a Re—Os isotopic age of 470 Ma (Walker et al., 2002). Analysis of primary inclusions of platinum-group minerals (PGM) in the chromite (Garuti et al., 1999; Pasava et al., 2011; Walker et al., 2002) have shown that fluid played an important role in chromitite formation (Garuti et al., 1999).

3. Red corundum-bearing vein

3.1. Occurrence of the red-corundum-bearing vein

This sampling location is ~150 m to the west of the No. 9 chromite ore body (known as the '*Tsentralnoe chromite deposite*'; Bryanchaninova et al., 2004; Makeyev, 2006). Given that the red-corundum-bearing vein has been completely mined, samples were collected from the waste quarry (66°51′34″N and 65°14′44″E; Fig. 1b), where the original vein was lenticular and 20 m long and 7 m wide (Bryanchaninova et al., 2004; Ishimaru et al., 2015) and abandoned pit is covered with snow (Fig. 1c). The red-corundum-bearing rocks occur in the mica zone of the vein (Fig. 2a, d; Bryanchaninova et al., 2004; Makeyev, 2006). The wall-rock of the vein consists of dunite–harzburgite, which is zoned from fine- to medium-grained dunite, to fine-grained dunite, and finally harzburgite (Fig. 2b).

3.2. Samples of red-corundum-bearing rocks

The samples have blastic textures and consist of red corundum (10%–35%), oligoclase (40%–50%), phlogopite (20%–35%), paragonite (5%–10%), and chromian spinel (5%–15%), with varying mineral proportions between samples (Fig. 2d).

The corundum occurs as light–dark pink, fine to coarse crystal sizes (3–10 mm) with hexagonal cross-sections, and is an interstitial phase between oligoclase and phlogopite (Fig. 2d). Corundum crystals in the matrix are 0.2–0.6 mm in size, occur as an interstitial phase of oligoclase and phlogopite, and are locally aligned (Fig. 3). Some red corundum grains contain chromian spinel inclusions (Fig. 4a, b), or are found as intergrowths with paragonite and phlogopite (Fig. 4c, d).

Oligoclase is white, prismatic, or xenomorphic granular, 1–3 mm in size, and contains fine inclusions of chromian spinel and phlogopite. Phlogopite is light brown, flaky, ~1–2 mm in size, and commonly occurs as an interstitial phase of oligoclase. It locally forms monomineralic domains (glimmerite). Paragonite crystals are light green and occur as an interstitial phase of phlogopite or as overgrowths around red corundum. Minor paragonite contains chromian spinel inclusions (Fig. 3d). Chromian spinel is dark brown and anhedral, and can be divided into coarse (2–4 mm) and fine (0.1–0.2 mm) grains (Fig. 3b, d). Fine-grained chromian spinel occurs as inclusions in oligoclase and phlogopite.

4. Analytical methods

Mineral compositions were obtained using a JXA8100 electron microprobe with an accelerating voltage of 20 kV, beam current 2×10^{-8} A, and beam diameter of 5 μm at the EPMA Laboratory, Institute of Geology, Chinese Academy of Geological Sciences (CAGS), Beijing, China.

Zircons were separated from the oligoclasite using standard heavy liquid and magnetic techniques, handpicked under a binocular microscope, and mounted in epoxy resin. The sample mount was polished to expose the cores of zircon grains. The internal structures of zircon were imaged by cathodoluminescence (CL) using a scanning electron microscope (FEI PHILIPS XL30 SEFG) with a 2 min scanning time at

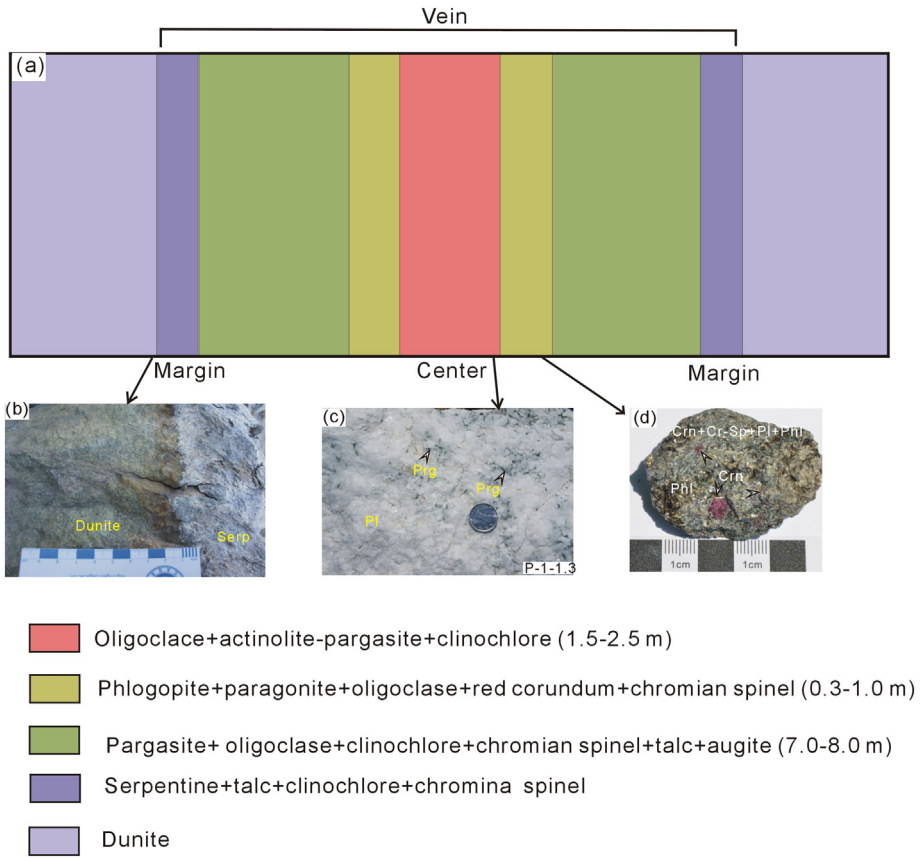

Fig. 2. Mineralogical zones and representative rocks of red-corundum-bearing vein. (a) Reconstructed profile of the red-corundum-bearing vein (see Bryanchaninova et al., 2004; Ishimaru et al., 2015); (b) contact relationship between vein (serp.) and wall rock (dunite); (c) Oligoclasite in center zone, zircons were separated from the oligoclasite for this study; (d) Hand specimens of the red-corundum-bearing rocks (C-4-1), consists of Crn, Cr-Sp, Pl and Phl. Abbreviations:Serp-serpentine, Prg-pargasite, Crn-red corundum, Cr-Sp-chromian spinel, Pl-oligoclase, Phl-phlogopite.

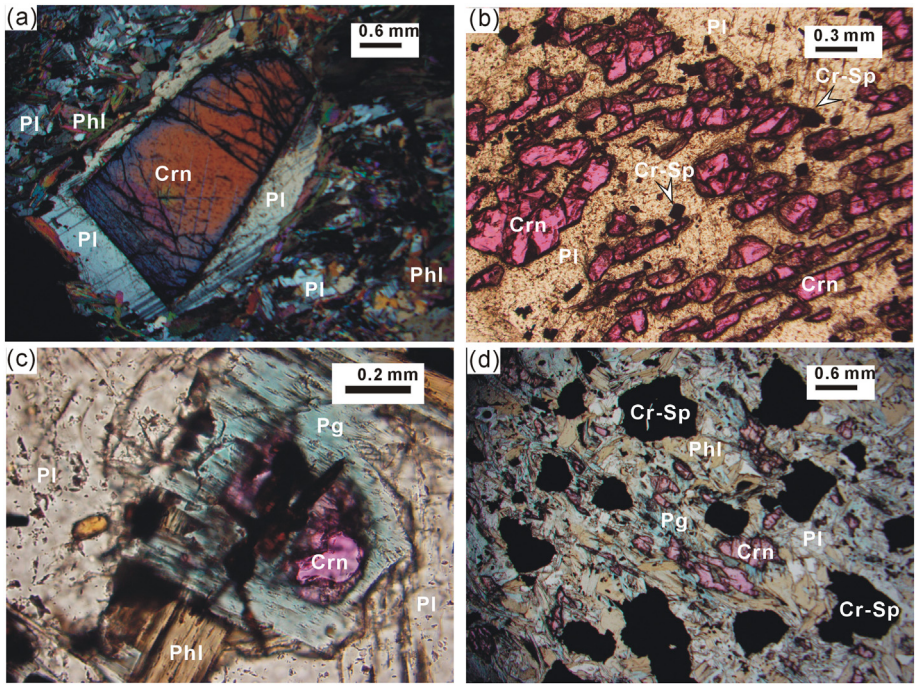

Fig. 3. Photomicrographs of red-corundum-bearing rocks from Rai-Iz ultramafic rocks, the Polar Urals, Russia. (a) Pl grown surrounding coarse-grained Crn. Pl ring showing accordant crystallography orientation, fine grained Pl and Phl inhabit in matrix (crossed polars) (C-3). (b) Fine-grained Crn (pink) directionally distributed in the matrix, some tiny chromian spinel appearing in the Pl (C-1). (c) Pg grown surrounding red corundum, neighboring with Phl and Pl (C-1). (d) Assemblage of Cr-Sp, Crn, Pl, Phl and Pg (C-5). Abbreviations: Pg-paragonite, other minerals as Fig. 2. (b), (c) and (d) under plane-polarized light.

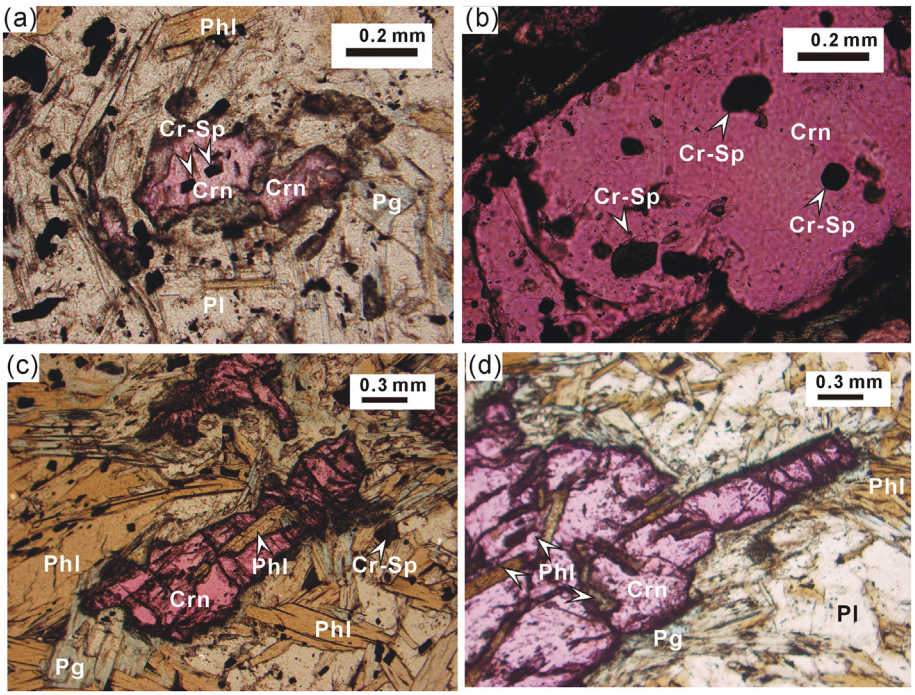

Fig. 4. Structure relationship between red corundum and other minerals in the red-corundum-bearing rocks. (a) and (b): irregular or round chromian spinel inclusions in Crn (C-1; C-5). (c) and (d): Phl growing along crevasse of Crn (C-3; C-9). Abbreviations as Fig. 2.

conditions of 15 kV and 120 nA at the Beijing SHRIMP Centre, CAGS, Beijing, China.

Zircon dating was performed on a Neptune multicollector inductively coupled plasma mass spectrometer (MC–ICP–MS) with a 193 nm-FX ArF excimer laser ablation system at the Isotopic Laboratory, Tianjin Institute of Geology and Mineral Resources, Tianjin, China. All peaks were measured by ion counters due to the relatively low U concentration of zircons and the 20 μm laser spot diameter. NIST610 glass was used as an external standard to calculate zircon U, Th, and Pb concentrations, and TEMORA zircon was used as an external standard to normalize isotopic fractionation during analysis. The ^{208}Pb method was used for the common Pb correction (Andersen, 2002). Uncertainties of individual analyses are reported as 1σ errors, and weighted-mean ages are reported at the 2σ level. Isoplot 3.0 (Ludwig, 2003) was used for the age calculations and construction of concordia diagrams. The detailed analytical technique followed is described in Liu et al. (2010).

Zircon Hf isotope analyses were performed using a laser ablation microprobe (New Wave UP213) attached to a Neptune MC–ICP–MS at the Institute of Mineral Resources, CAGS, Beijing, China. Instrumental conditions and data acquisition procedures followed are described in Hou et al. (2007) and Wu et al. (2006). A stationary spot was used for the analyses, with a beam diameter of either 40 or 55 μm, depending on the size of the analyzed domains. The ablated sample was transported from the laser ablation cell using He carrier gas, then combined with Ar in a mixing chamber before entering the ICP–MS torch. Correction for the isobaric interferences of ^{176}Lu and ^{176}Yb with ^{176}Hf utilized ^{176}Lu/^{175}Lu = 0.02658 and ^{176}Yb/^{173}Yb = 0.796218 (Chu et al., 2002). For instrumental mass bias correction, Yb isotope ratios were normalized to ^{172}Yb/^{173}Yb = 1.35274 (Chu et al., 2002) and Hf isotope ratios to ^{179}Hf/^{177}Hf = 0.7325, using an exponential law. The mass bias behavior of Lu was assumed to follow that of Yb; the mass bias correction protocols followed are described by Iizuka and Hirata (2005), Wu et al. (2006), and Hou et al. (2007). Zircon GJ1 was used as the reference standard, which yielded a weighted-mean ^{176}Hf/^{177}Hf ratio of 0.282008 ± 27 (2σ) during our analyses. This ratio is within uncertainty of the weighted-mean ^{176}Hf/^{177}Hf ratio of 0.282013 ± 19 (2σ) derived from in situ analysis by Elhlou et al. (2006).

Fresh phlogopite was handpicked under a binocular microscope to remove altered crystals and ensure an estimated purity of >99%. The packaged samples of 0.18–0.28 mm were irradiated in a vacuum within a Cd-coated quartz vial for 24 h (at the Chinese Academy of Atomic Energy Sciences, Beijing, China) with an integral neutron flux of 2.22048 × 10^{18} n/cm^2 s. Chinese Standard ZBH-25 (biotite, age of 132.7 Ma) was used as the neutron fluence monitor. Interfering nucleogenic reactions were checked for every irradiation by using CaF and K_2SO4. The correction factors used in this study were $[^{36}Ar/^{37}Ar]_{Ca}$ = 0.000271, $[^{39}Ar/^{37}Ar]_{Ca}$ = 0.000652, and $[^{40}Ar/^{39}Ar]_{K}$ = 0.00703.

^{40}Ar/^{39}Ar step-heating measurements were performed at the Key Laboratory of Orogen and Crust Evolution (KLOCE), Peking University, Beijing, China. Samples were placed into a Ta tube resting in the Ta crucible of an automated double-vacuum resistance furnace, and incrementally heated from 800 °C to 1500 °C in 10–15 steps of 20 min each. This was followed by 20, 15, and 10 min of gas purification on sponge Ti getters, Zr–V–Fe getters, and activated carbon getters, respectively. Isotopic measurements were made on a mass spectrometer (RGA10) with a Faraday cup and an electron multiplier (the latter was used as the collector during this study). Ar isotopic data were corrected using the ^{40}Ar/^{39}Ar Dating 1.2 program (KLOCE), and plateau and isochron ages were calculated using Isoplot 3.0 (Ludwig, 2003). The detailed analytical technique followed is described by Gong et al. (2006).

5. Results

5.1. Mineral chemistry

5.1.1. Red corundum

Coarse-grained prophyroblast corundum is characterized by 95.2–97.7 wt% Al_2O_3 and 1.8–3.6 wt% Cr_2O_3. Fine-grained corundum in the matrix is characterized by 92.3–96.1 wt% Al_2O_3 and 2.1–6.9 wt% Cr_2O_3 (Table 1).

Table 1
Representative analyses of corundum from red-corundum-bearing rock in the Rai-Iz ultramafic rocks, Polar Ural, Russia.

Samples	C-1						C-3			C-6			C-5		
Crystal	M	M	M	M	M	M	P	P	P	P	M	M	M	M	M
Point	1-1-1	1-1-2	1-2-27	1-2-28	1-4-46	1-5-61	3-1-82	3-1-84	3-1-96	6-2-107	6-3-109	6-3-111	5-3-163	5-3-164	5-3-165
SiO_2	0.02	bdl	0.06	0.02	0.01	0.01	bdl	0.01	0.01	bdl	0.03	0.02	0.01	bdl	bdl
TiO_2	0.04	0.01	0.03	0.06	0.06	bdl	0.02	0.03	bdl	bdl	0.03	0.02	bdl	bdl	0.02
Al_2O_3	92.65	92.35	96.40	93.27	96.32	95.08	96.08	95.23	96.69	96.09	94.70	95.39	97.54	97.73	96.85
Cr_2O_3	6.13	6.93	3.32	5.79	4.04	4.69	2.58	3.29	2.56	3.49	4.45	3.38	2.30	1.85	3.05
FeO	0.46	0.48	0.38	0.49	0.37	0.40	0.37	0.40	0.36	0.42	0.51	0.41	0.42	0.30	0.47
MnO	bdl	0.02	0.02	bdl	0.02	0.01	bdl	0.02	0.01	0.01	0.01	bdl	bdl	0.03	bdl
MgO	bdl	0.01	bdl	0.02	bdl	bdl	0.02	0.01	bdl	bdl	bdl	bdl	bdl	bdl	0.01
CaO	0.01	0.02	bdl	0.01	0.03	bdl	0.01	bdl	0.02	bdl	bdl	bdl	bdl	0.03	0.01
Na_2O	bdl	0.03	bdl	0.01	bdl	bdl	0.01	0.02	bdl	0.02	bdl	bdl	bdl	bdl	bdl
K_2O	0.01	bdl	0.01	0.01	bdl	0.01	bdl	bdl	bdl	0.02	0.01	bdl	bdl	bdl	bdl
NiO	bdl	bdl	0.01	bdl	bdl	bdl	bdl	bdl	bdl	bdl	bdl	bdl	bdl	0.02	bdl
SrO	0.03	0.13	0.04	0.10	0.01	0.03	0.04	bdl	0.03	0.06	0.06	0.01	0.11	bdl	0.03
BaO	0.02	0.04	0.09	bdl	0.04	0.01	0.03	bdl	bdl	bdl	bdl	bdl	0.02	bdl	0.03
Total	99.38	100.02	100.36	99.78	100.90	100.25	99.15	99.00	99.69	100.10	99.80	99.23	100.40	99.97	100.47
Numbers of ions on the basis of 3 O															
Si	0.000	0.000	0.001	0.000	0.000	0.000	0.000	0.000	0.000	0.000	0.001	0.000	0.000	0.000	0.000
Ti	0.000	0.000	0.000	0.001	0.001	0.000	0.000	0.000	0.000	0.000	0.000	0.000	0.000	0.000	0.000
Al	1.908	1.896	1.947	1.911	1.939	1.930	1.959	1.948	1.960	1.946	1.931	1.948	1.963	1.970	1.952
Cr	0.085	0.095	0.045	0.080	0.055	0.064	0.035	0.045	0.035	0.047	0.061	0.046	0.031	0.025	0.041
Fe^{3+}	0.006	0.006	0.005	0.006	0.005	0.005	0.005	0.005	0.005	0.005	0.007	0.005	0.005	0.004	0.006
Mn	0.000	0.000	0.000	0.000	0.000	0.000	0.000	0.000	0.000	0.000	0.000	0.000	0.000	0.000	0.000
Mg	0.000	0.000	0.000	0.001	0.000	0.000	0.000	0.000	0.000	0.000	0.000	0.000	0.000	0.000	0.000
Ca	0.000	0.000	0.000	0.000	0.000	0.000	0.000	0.000	0.000	0.000	0.000	0.000	0.000	0.001	0.000
Na	0.000	0.001	0.000	0.000	0.000	0.000	0.000	0.001	0.000	0.001	0.000	0.000	0.000	0.000	0.000
K	0.000	0.000	0.000	0.000	0.000	0.000	0.000	0.000	0.000	0.000	0.000	0.000	0.000	0.000	0.000
Ni	0.000	0.000	0.000	0.000	0.000	0.000	0.000	0.000	0.000	0.000	0.000	0.000	0.000	0.000	0.000
Sr	0.000	0.001	0.000	0.001	0.000	0.000	0.000	0.000	0.000	0.001	0.001	0.000	0.001	0.000	0.000
Ba	0.000	0.000	0.001	0.000	0.000	0.000	0.000	0.000	0.000	0.000	0.000	0.000	0.000	0.000	0.000
Total	2.000	2.000	1.999	1.999	2.000	2.000	2.000	2.000	2.000	2.000	1.999	2.000	1.999	2.000	2.000

P- porphyritic, M- matrix, bdl-below detection limit.

5.1.2. Chromian spinel

Coarse-grained chromian spinel from the vein is Cr-rich and Al-poor, being characterized by 37.8–54.7 wt% Cr_2O_3, 10.5–26.9 wt% Al_2O_3, and 24.1–29.5 wt% FeO. Fine-grained chromian spinel is Cr-poor and Al-rich, with 35.3–41.3 wt% Cr_2O_3, 22.5–27.2 wt% Al_2O_3, and 27.1–30.2 wt % FeO (Table 2; Fig. 5). The coarse-grained chromian spinel is zoned, with increasing Al_2O_3 and decreasing Cr_2O_3 contents from core to rim (Fig. 6).

5.1.3. Oligoclase

Oligoclase is characterized by 61.0–62.6 wt% SiO_2, 23.1–24.1 wt% Al_2O_3, 4.7–5.4 wt% CaO, and 7.9–8.4 wt% Na_2O (Table 3). Anorthite

Table 2
Representative analyses of chromian Spinel from red-corundum-bearing rock in the Rai-Iz ultramafic rocks, Polar Ural, Russia.

Samples	C-1			C-3		C-6			C-5				
Point	1-1-13	1-1-19	1-1-22	3-1-80	3-1-81	6-1-97	6-7-144	6-7-145	5-1-152	5-2-157	5-2-158	5-4-183	5-4-184
Occurrece	fine	coarse/c	coarse/r	fine	fine	coarse	coarse/c	coarse/r	coarse	coarse/c	coarse/r	coarse	coarse
Cr_2O_3	39.30	54.76	50.22	35.33	38.59	52.02	54.76	39.60	54.15	51.34	41.31	52.66	54.23
Al_2O_3	25.80	12.23	16.00	27.85	23.99	13.57	10.17	22.01	11.29	13.88	23.91	13.19	11.05
TiO_2	0.06	0.00	0.04	0.00	0.05	0.06	0.12	0.00	0.04	0.02	0.00	0.00	0.02
FeO	26.75	28.09	27.80	30.23	28.99	30.79	29.98	29.55	27.57	27.48	25.46	26.95	27.37
MgO	6.98	5.34	5.82	5.22	5.30	3.56	3.85	6.99	4.66	5.19	7.67	5.04	4.93
MnO	0.34	0.47	0.45	0.45	0.52	0.62	0.63	0.52	0.87	0.82	0.66	0.83	0.85
NiO	0.00	0.00	0.00	0.02	0.05	0.00	0.02	0.02	0.04	0.01	0.04	0.05	0.05
Total	99.22	100.89	100.33	99.08	97.48	100.61	99.53	98.68	98.62	98.73	99.05	98.73	98.48
Numbers of ions on the basis of 32 O													
Cr	7.938	11.718	10.582	7.180	8.086	11.230	12.124	8.257	11.931	11.131	8.398	11.446	11.963
Al	7.770	3.901	5.029	8.441	7.495	4.370	3.356	6.845	3.708	4.486	7.247	4.275	3.634
Ti	0.011	0.000	0.009	0.000	0.011	0.013	0.025	0.000	0.009	0.003	0.001	0.000	0.003
Fe^{3+}	0.357	0.504	0.491	0.501	0.526	0.494	0.622	1.176	0.453	0.498	0.468	0.369	0.525
Fe^{2+}	5.360	5.855	5.706	5.998	5.898	6.537	6.399	5.342	5.973	5.804	5.008	5.828	5.862
Mg	2.660	2.154	2.313	1.998	2.091	1.448	1.608	2.746	1.934	2.120	2.939	2.065	2.051
Mn	0.038	0.058	0.056	0.068	0.081	0.094	0.098	0.080	0.153	0.143	0.107	0.145	0.150
Ni	0.000	0.000	0.000	0.004	0.010	0.000	0.005	0.005	0.009	0.003	0.009	0.011	0.011
Total	24.135	24.191	24.186	24.190	24.199	24.187	24.236	24.449	24.171	24.188	24.177	24.139	24.199
Mg#	31.81	48.70	41.49	22.36	26.12	30.40	42.53	36.87	46.20	42.44	37.41	43.26	49.64
Cr#	50.53	75.02	67.79	45.97	51.89	71.99	78.32	54.68	76.29	71.27	53.68	72.81	76.70
Fe#	0.25	0.29	0.30	0.26	0.29	0.19	0.27	0.87	0.23	0.28	0.36	0.20	0.28

$Mg^{\#} = 100Mg/Mg+Fe^{2+}$; $Cr^{\#} = 100Cr/Cr+Al$; $Fe^{\#} = 100Fe^{3+}/Cr+Al+Fe^{3+}$; c- core, r-rim

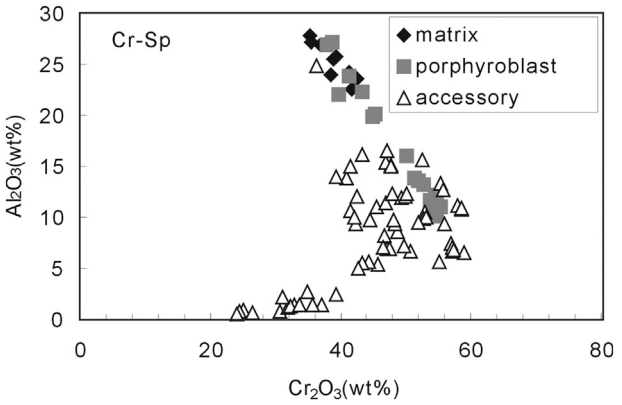

Fig. 5. Diagram of Al_2O_3 (wt%) vs. Cr_2O_3 (wt%) variation of chromian spinel. Data of accessory chromian spinel from Rai-Iz ultramafic rocks after Makeyev and Bryanchaninova (1999).

(An) contents vary from 20 to 30, and decrease from core to rim (from 28 to 27 to 25–20 for different crystals). Oligoclase also occurs as inclusions in the chromian spinel, which has varying An contents of 23–28, similar to oligoclase in the matrix. Only one anorthite grain was analyzed, which was an inclusion in oligoclase, and characterized by a near pure An composition (An = 99; Table 3).

5.1.4. Phlogopite

Phlogopite from the matrix is characterized by 36.9–41.1 wt% SiO_2, 15.8–21.4 wt% Al_2O_3, 18.7–21.7 wt% MgO, 6.0–8.1 wt% K_2O, and 1.3–2.4 wt% Na_2O (Table 4). Mg# values [100 Mg/(Mg + Fe)] of phlogopite are 88–94 (Fig. 7a). Phlogopite has high BaO contents of 0.8–2.7 wt% (Fig. 7b). The Al_2O_3, MgO, and Na_2O contents decrease with increasing K_2O and BaO contents from core to rim. Inclusions of phlogopite in oligoclase, corundum, and chromian spinel have similar compositions to those from the matrix (Table 4; Fig. 7).

5.1.5. Paragonite

Paragonite in the matrix is characterized by 41.1–42.1 wt% SiO_2, 38.2–40.2 wt% Al_2O_3, and 5.3–6.4 wt% Na_2O. Both MgO and K_2O contents are <1.0 wt%. SiO_2, Al_2O_3, and Na_2O contents increase with decreasing SrO content away from corundum (Table 4; Fig. 3c).

5.2. Zircon from oligoclasite

5.2.1. Zircon dating

>1000 zircons were separated from 5 kg of oligoclasite (sample P-1-1.3; Fig. 2b). They are colorless to light yellow, mostly idiomorphic and prismatic, 100–300 μm long, 100–150 μm wide, and have length:width ratios of 1:3. Most zircons are free from inclusions and some have fractures. Most of the zircons display oscillatory and sector zoning in CL images (e.g., numbers 1 and 17; Fig. 8), and some have overgrowth rims (e.g., number 14; Fig. 8), suggesting that these zircons grew in a melt or fluid (Corfu et al., 2003). The analyzed zircons have U = 70–501 ppm and Th/U = 0.07–0.25 (Table 5). Twenty zircons were analyzed by LA–MC–ICP–MS, and 19 analyses yielded $^{206}Pb/^{238}U$ ages of 389–372 Ma, with the exception of one zircon (number 5) with an older age of 429 ± 2 Ma (Table 5; Fig. 8). Nineteen concordant ages yield a weighted-mean $^{206}Pb/^{238}U$ age of 382 ± 2 Ma (MSWD = 1.4; Fig. 9).

5.2.2. Zircon Lu—Hf isotopes

Lu—Hf isotopes were analyzed in 27 zircons by LA–MC–ICP–MS (Table 6), which yielded 20 U–Pb ages (Fig. 9). The zircons have $^{176}Lu/^{177}Hf$ ratios of 0.00004–0.001 and $^{176}Hf/^{177}Hf$ ratios of 0.282056–0.282855, corresponding to εHf(0) values of −19.4 to +3.2. Their εHf(t) values range from −11.2 to +12.6 (Fig. 10): 4 zircons have negative εHf(t) values (−11 to −8), 11 zircons have low positive values (0 to +5), 8 zircons have moderate positive values (+5 to +10), and 3 zircons have high positive values (+11 to +13) (Table 6).

5.3. $^{40}Ar/^{39}Ar$ dating

$^{40}Ar/^{39}Ar$ analyses were performed on phlogopite separated from sample PU-6 (Table 7). The results yielded a plateau age of 377 ± 2 Ma (2σ; MSWD = 1.16) and an isochron age of 377 ± 3 Ma (MSWD = 0.44) (Fig. 11), which represent crystallization age of the phlogopite and constrain the latest precipitation time of the red-corundum-bearing vein.

6. Discussion

Metasomatic models (Bryanchaninova et al., 2004; Goldny et al., 2003; Ishimaru et al., 2015; Makeyev, 2006) and a metamorphic differentiation model (Vakhrusheva et al., 2016) have been proposed to explain the genesis of the red-corundum-bearing vein in the Rai–Iz peridotite. The data presented in Section 5 support the first model and indicate that subduction fluids were the source of the vein (Goldny et al., 2003; Ishimaru et al., 2015).

6.1. Age of the red-corundum-bearing vein

Zircons from the oligoclasite yielded a weighted-mean $^{206}Pb/^{238}U$ age of 382 ± 2 Ma (Fig. 9), indicating the crystallization age of the vein. $^{40}Ar/^{39}Ar$ analysis of phlogopite separated from the red-corundum-bearing vein yielded a plateau age of 377 ± 3 Ma (Table 7; Fig. 11), representing a minimum formation age of the vein. They are consistent within the errors. A Rb/Sr mineral isochron age of 373 ± 5 Ma was obtained by Goldny et al. (2003). The earliest formation age of the red-corundum-bearing vein is 380 Ma, on the basis of the above $^{206}Pb/^{238}U$, $^{40}Ar/^{39}Ar$, and Rb/Sr ages. Vakhrusheva et al. (2016) reported $^{206}Pb/^{238}U$ ages ranging from 415 ± 4 to 386 ± 7 Ma for the red-corundum-bearing oligoclase-rich rocks (nine zircons analyzed by SHRIMP; sample Y-292/2). Their analyses yielded Th/U ratios of 0.13–0.24 and a weighted-mean age of 404 ± 3 Ma, representing the formation age of these rocks (Vakhrusheva et al., 2016). Their youngest age of 386 ± 7 Ma is within error of our results (Table 5; Fig. 9), but their data have higher Th/U ratios (Table 5), possibly reflecting different environments of zircon crystallization for the two samples (Harley et al., 2007). If 400

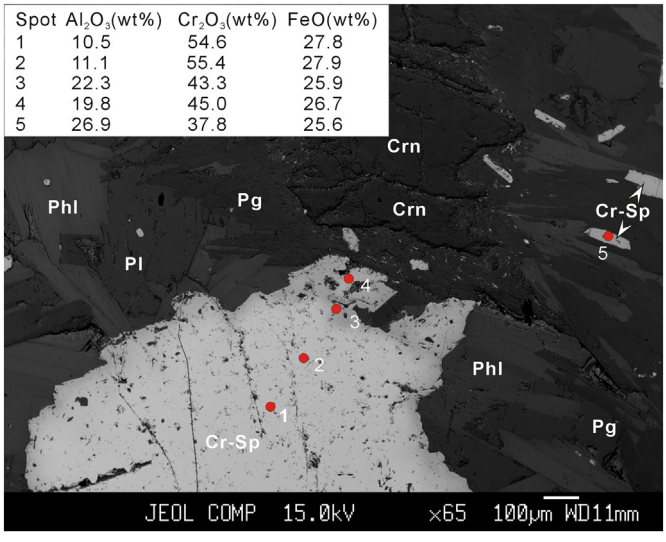

Fig. 6. Backscattered electron images (BSE) of red-corundum-bearing rocks and composition zone of the chromian spinel (C-5). Sample Abbreviations as Fig. 2.

Table 3
Representative analyses of plagioclase from red-corundum-bearing rock in the Rai-Iz ultramafic rocks, Polar Ural, Russia.

Sample	C-1						C-6		C-5		
Position	R	C	R	C	M	R	Inc	C	Inc	C	Inc
Point	1-1-10	1-1-11	1-1-12	1-4-57	1-4-58	1-4-59	6-4-124	6-4-129	5-1-146	5-3-168	5-4-177
SiO_2	61.45	60.80	61.49	60.95	61.78	63.32	40.16	61.72	62.62	61.79	61.98
TiO_2	0.03	0.01	0.02	0.00	0.00	0.00	0.18	0.00	0.00	0.01	0.03
Al_2O_3	23.98	24.14	23.54	24.10	23.28	22.55	28.48	23.12	23.19	23.40	23.32
Cr_2O_3	0.01	0.04	0.06	0.01	0.00	0.00	1.92	0.00	0.17	0.05	0.09
FeO	0.02	0.04	0.08	0.00	0.03	0.00	3.25	0.04	0.14	0.02	0.07
MnO	0.00	0.02	0.02	0.01	0.00	0.00	0.06	0.00	0.01	0.00	0.00
MgO	0.01	0.00	0.01	0.00	0.00	0.01	0.07	0.02	0.00	0.00	0.00
CaO	5.11	5.64	5.13	5.49	4.61	4.17	22.80	4.19	4.72	5.36	5.09
Na_2O	8.30	8.15	8.41	8.18	8.21	8.95	0.00	8.89	8.66	7.92	8.05
K_2O	0.03	0.02	0.03	0.01	0.04	0.05	0.03	0.01	0.03	0.04	0.03
NiO	0.00	0.03	0.00	0.00	0.04	0.00	0.03	0.00	0.00	0.00	0.00
SrO	0.88	0.68	1.15	0.53	1.09	0.93	2.45	1.05	0.52	0.76	0.98
BaO	0.03	0.06	0.07	0.09	0.00	0.07	0.01	0.10	0.03	0.02	0.06
Total	99.85	99.63	99.99	99.36	99.08	100.04	99.44	99.14	100.09	99.36	99.71
Numbers of ions on the basis of 8 O											
Si	2.739	2.720	2.745	2.729	2.771	2.810	1.972	2.772	2.777	2.763	2.765
Ti	0.001	0.000	0.001	0.000	0.000	0.000	0.006	0.000	0.000	0.000	0.001
Al	1.260	1.273	1.239	1.272	1.231	1.179	1.648	1.223	1.212	1.233	1.227
Cr	0.000	0.001	0.002	0.000	0.000	0.000	0.075	0.000	0.006	0.002	0.003
Fe^{3+}	0.001	0.001	0.003	0.000	0.001	0.000	0.120	0.001	0.005	0.001	0.002
Mn	0.000	0.001	0.001	0.000	0.000	0.000	0.002	0.000	0.001	0.000	0.000
Mg	0.001	0.000	0.001	0.000	0.000	0.000	0.005	0.001	0.000	0.000	0.000
Ca	0.244	0.271	0.245	0.263	0.222	0.198	1.199	0.202	0.224	0.257	0.243
Na	0.718	0.707	0.728	0.710	0.714	0.770	0.000	0.774	0.745	0.686	0.696
K	0.002	0.001	0.002	0.001	0.002	0.003	0.002	0.001	0.002	0.002	0.002
Ni	0.000	0.001	0.000	0.000	0.002	0.000	0.001	0.000	0.000	0.000	0.000
Sr	0.023	0.018	0.030	0.014	0.028	0.024	0.070	0.027	0.013	0.020	0.025
Ba	0.001	0.001	0.001	0.002	0.000	0.001	0.000	0.002	0.001	0.000	0.001
Total	4.965	4.977	4.966	4.975	4.942	4.961	5.031	4.974	4.971	4.943	4.940
Ab	74.50	72.24	74.67	72.89	76.14	79.31	0.00	79.28	76.70	72.60	73.96
An	25.34	27.64	25.16	27.05	23.64	20.41	99.84	20.66	23.11	27.19	25.87
Or	0.17	0.12	0.18	0.05	0.23	0.28	0.16	0.06	0.19	0.21	0.17

R-rim, M-mantle, C-core, Inc-inclusion, total Fe as Fe_2O_3.

Ma represents the true formation age, then two generations of oligoclase-rich rocks or protoliths existed, which requires further study. The Sob plagiogranite located in the southeast area near the Voykar Massif has yielded a SHRIMP zircon U—Pb age of 395 ± 5 Ma (Udoratina et al., 2008), and therefore formed ~10 Myr earlier than the vein. Hence, the granite was not the source of the fluid that formed the red-corundum-bearing vein.

6.2. Evidence for hydrothermal formation of the red-corundum-bearing vein

6.2.1. Mineralogical zones

The following mineralogical zones can be divided according to the degree of concentration of the main mineral for the red-corundum-bearing vein (from center to margin; Fig. 2a): oligoclase, red-corundum-bearing phlogopite, pargasite, and serpentine (due to the metasomatic alteration of dunite; Bryanchaninova et al., 2004). These zones are the result of interaction between fluids and dunite. Similar zones are found in the dunite-hosted corundum-bearing vein at the Corundum Hill mine, North Carolina, USA, and are related to the hydrothermal replacement of dunite (corundum, spinel-bearing chlorite, chlorite, orthopyroxene, talc, and dunite zones from center to margin; Pratt, 1906; Hadley, 1949). Fluid interaction with peridotite can also form other mineralogical zones, such as the peridotite-hosted jadeitite of Tawmaw (Myanmar), with jadeite, albite, chlorite, and serpentine zones from center to margin (Harlow and Sorensen, 2005). Therefore, mineralogical zones are commonly observed due to the interaction between fluid and peridotite. In addition, phase relations of the peridotite + fluid system show the appearance of phlogopite, amphibolite, talc, and serpentine as temperature gradually decreases (Peacock, 1990). Thus, the mineralogical zones of the red-corundum-bearing vein indicate an origin from hydrothermal fluids.

6.2.2. Whole-rock Sr—Nd isotopic compositions

Based on whole-rock initial $^{87}Sr/^{86}Sr$ (0.704846) and $^{143}Nd/^{144}Nd$ (0.512327) ratios, Goldny et al. (2003) calculated εNd (380 Ma) values of +3.3 for the red-corundum-bearing rock, and these Sr—Nd isotopic data indicate that the fluid was derived from dehydration of a subducted slab. Its Sr—Nd isotopic compositions are distinctly different from those of the Marun–Keu eclogite and gneiss in the area 100 km northeast of the Rai–Iz massif, which are the subducted and metamorphic products of arc igneous rocks (Glodny et al., 2004; Goldny et al., 2003). The εNd values of harzburgite and dunite from the Rai–Iz ultramafic massif are +6.4 and + 6.6 (400 Ma), respectively (Ronkin et al., 2000). They are higher than those of the red-corundum-bearing vein, which does not support genesis via reactions between ultramafic rocks and magmatic water (Bryanchaninova et al., 2004; Makeyev, 2006), or the model of metamorphic differentiation of ultramafic rocks (Vakhrusheva et al., 2016). Therefore, we conclude that the fluid was derived from subducted oceanic crust rather than from the Marun–Keu eclogite and gneiss or the Rai–Iz harzburgite and dunite. The interaction between peridotite and fluid derived from subducted sediment can form veins with low εNd(t) values, such as the high-pressure veins in the Franciscan complex in California, USA, and those in the west Tianshan eclogites, NW China (Huang et al., 2005; Nelson, 1991, 1995).

6.2.3. Mineralogical records

Zircons exhibit obvious oscillatory zoning (Fig. 8) and Th/U ratios that are mostly <0.2 (Table 5). These features are similar to

Table 4
Representative analyses of Paragonite and phlogopite from red -corundum-bearing rock in the Rai-Iz ultramafic rocks, Polar Ural, Russia.

Samples	C-1										C-3			
Point	1-1-4.	1-1-6.	1-1-16.	1-2-29	1-4-47	1-4-48	1-4-52	1-4-54	1-5-66	1-5-68	3-1-71	3-1-73	3-1-86	3-1-91
Mineral	Pg	Pg	Pg	Phl	Pg	Pg	Phl	Phl	Pg	Pg	Phl	Phl	Phl	Phl
SiO_2	42.32	43.56	42.74	36.99	42.15	42.59	37.44	37.16	42.10	43.56	37.25	37.41	37.95	41.08
TiO_2	0.15	0.15	0.25	1.28	0.23	0.20	1.08	1.20	0.18	0.14	0.63	0.54	0.64	0.58
Al_2O_3	39.38	40.13	38.24	20.11	37.28	38.14	20.44	20.29	39.86	40.22	20.56	20.49	20.30	15.75
Cr_2O_3	1.46	0.37	1.78	2.22	2.52	2.25	2.33	2.33	0.43	0.03	1.83	1.93	1.84	1.73
FeO	0.35	0.26	0.40	3.53	0.45	0.45	3.51	3.49	0.42	0.26	4.44	4.36	4.76	4.37
MnO	0.04	0.02	0.01	0.01	0.00	0.00	0.00	0.02	0.00	0.00	0.04	0.04	0.00	0.02
MgO	0.89	0.68	0.53	19.25	0.80	0.75	19.37	19.18	0.82	0.39	18.72	19.13	19.16	21.74
CaO	1.42	1.50	1.17	0.04	1.13	1.08	0.00	0.02	1.68	1.47	0.00	0.03	0.07	0.02
Na_2O	6.20	6.42	6.00	2.05	5.84	5.92	2.40	2.23	5.88	6.02	2.11	2.02	2.03	1.29
K_2O	0.33	0.16	0.43	6.46	0.45	0.45	6.18	6.01	0.35	0.29	6.64	6.79	6.37	7.23
NiO	0.00	0.00	0.00	0.05	0.04	0.02	0.03	0.13	0.00	0.04	0.07	0.08	0.05	0.11
SrO	1.75	1.06	2.10	0.09	2.32	2.23	0.00	0.06	1.84	1.94	0.00	0.01	0.07	0.02
BaO	0.34	0.10	0.69	2.38	0.56	0.63	2.76	2.93	0.44	0.33	1.77	1.34	2.05	1.39
Total	94.63	94.41	94.33	94.47	93.77	94.71	95.52	95.07	93.98	94.69	94.07	94.16	95.28	95.32
Numbers of ions on the basis of 24 O														
Si	5.583	5.684	5.680	5.321	5.659	5.651	5.329	5.322	5.580	5.699	5.368	5.370	5.405	5.810
Al ^{iv}	2.417	2.316	2.320	2.679	2.341	2.349	2.671	2.678	2.420	2.301	2.632	2.630	2.595	2.190
Al ^{vi}	3.706	3.858	3.671	0.731	3.558	3.616	0.757	0.748	3.808	3.901	0.861	0.838	0.813	0.436
Ti	0.015	0.015	0.024	0.139	0.023	0.020	0.115	0.129	0.018	0.014	0.068	0.058	0.069	0.062
Cr	0.153	0.039	0.187	0.253	0.268	0.236	0.262	0.264	0.045	0.003	0.209	0.219	0.207	0.193
Fe	0.039	0.028	0.045	0.425	0.051	0.050	0.418	0.418	0.046	0.028	0.535	0.523	0.567	0.517
Mn	0.004	0.002	0.001	0.001	0.000	0.000	0.000	0.003	0.000	0.000	0.005	0.004	0.000	0.003
Mg	0.174	0.133	0.105	4.127	0.159	0.148	4.109	4.094	0.162	0.077	4.022	4.094	4.067	4.585
Ca	0.200	0.210	0.167	0.006	0.162	0.154	0.001	0.004	0.239	0.206	0.001	0.004	0.011	0.003
Na	1.586	1.624	1.547	0.573	1.521	1.522	0.662	0.619	1.510	1.528	0.590	0.562	0.560	0.354
K	0.056	0.027	0.073	1.186	0.076	0.076	1.121	1.099	0.059	0.048	1.221	1.243	1.158	1.305
Sr	0.134	0.080	0.162	0.008	0.181	0.171	0.000	0.005	0.141	0.147	0.000	0.001	0.006	0.002
Ba	0.018	0.005	0.036	0.134	0.029	0.033	0.154	0.164	0.023	0.017	0.100	0.076	0.115	0.077
Total	14.085	14.020	14.016	15.583	14.029	14.026	15.599	15.548	14.051	13.968	15.611	15.622	15.573	15.535
Mg#	0.818	0.825	0.701	0.907	0.757	0.748	0.908	0.907	0.777	0.731	0.883	0.887	0.878	0.899

Samples	C-6									C-5				
Point	6-1-101	6-1-102	6-3-113	6-3-115	6-3-116	6-4-122	6-4-123	6-6-139	6-6-140	5-1-150	5-2-159	5-2-160	5-3-170	5-4-180
Mineral	Phl	Phl	Pg	Phl	Phl	Phl	Phl	Phl	Phl	Phl	Phl	Pg	Phl	Phl
SiO_2	37.45	37.74	41.70	36.88	37.22	37.86	38.29	38.26	38.27	37.65	37.81	41.38	37.48	37.86
TiO_2	0.67	0.57	0.07	0.57	0.57	0.56	0.63	0.76	0.70	0.56	0.62	0.12	0.54	0.53
Al_2O_3	21.01	20.64	39.62	21.35	20.92	20.55	19.21	20.36	20.68	20.60	20.10	39.15	20.52	20.53
Cr_2O_3	1.90	1.89	1.54	1.83	1.99	1.72	2.17	2.10	1.96	2.43	2.06	1.63	1.74	1.95
FeO	3.84	4.02	0.47	4.36	4.37	4.62	3.74	3.19	3.59	2.59	2.89	0.35	2.74	2.61
MnO	0.00	0.03	0.00	0.02	0.04	0.02	0.02	0.04	0.03	0.05	0.02	0.00	0.00	0.00
MgO	20.06	19.87	0.79	19.31	19.78	19.82	20.62	19.94	19.84	21.15	20.61	0.60	21.00	21.01
CaO	0.00	0.04	2.23	0.03	0.03	0.01	0.01	0.11	0.06	0.02	0.13	2.39	0.01	0.00
Na_2O	1.99	2.20	5.77	2.01	1.92	1.73	1.40	1.81	2.06	1.92	1.74	5.28	1.87	1.81
K_2O	6.93	6.75	0.29	7.13	7.32	7.45	8.14	7.02	6.47	7.19	6.73	0.24	7.30	7.34
NiO	0.05	0.12	0.01	0.08	0.07	0.08	0.08	0.11	0.14	0.13	0.15	0.00	0.15	0.13
SrO	0.03	0.06	1.56	0.00	0.09	0.00	0.00	0.04	0.00	0.01	0.02	2.15	0.01	0.01
BaO	1.68	1.58	0.26	1.42	1.44	1.42	1.24	1.35	1.56	1.44	1.68	0.20	1.82	1.56
Total	95.60	95.50	94.31	94.97	95.76	95.83	95.56	95.08	95.35	95.73	94.55	93.46	95.19	95.34
Numbers of ions on the basis of 24 O														
Si	5.299	5.346	5.522	5.265	5.282	5.359	5.433	5.411	5.397	5.299	5.380	5.537	5.318	5.347
Al ^{iv}	2.701	2.654	2.478	2.735	2.718	2.641	2.567	2.589	2.603	2.701	2.620	2.463	2.682	2.653
Al ^{vi}	0.803	0.793	3.706	0.856	0.780	0.787	0.644	0.805	0.835	0.716	0.752	3.711	0.751	0.764
Ti	0.071	0.061	0.007	0.061	0.061	0.060	0.068	0.081	0.074	0.059	0.066	0.012	0.058	0.056
Cr	0.212	0.212	0.161	0.207	0.223	0.193	0.244	0.234	0.218	0.271	0.232	0.172	0.195	0.218
Fe	0.455	0.476	0.052	0.520	0.519	0.547	0.444	0.377	0.424	0.305	0.344	0.039	0.325	0.309
Mn	0.000	0.004	0.000	0.002	0.004	0.003	0.003	0.005	0.004	0.006	0.003	0.000	0.000	0.000
Mg	4.232	4.196	0.156	4.108	4.183	4.182	4.360	4.204	4.171	4.437	4.373	0.119	4.442	4.423
Ca	0.000	0.006	0.316	0.004	0.004	0.001	0.002	0.017	0.009	0.003	0.020	0.342	0.002	0.000
Na	0.545	0.603	1.482	0.556	0.529	0.475	0.386	0.496	0.563	0.524	0.479	1.370	0.515	0.495
K	1.252	1.219	0.049	1.297	1.325	1.345	1.473	1.267	1.164	1.290	1.221	0.040	1.322	1.323
Sr	0.002	0.005	0.120	0.000	0.007	0.000	0.000	0.003	0.000	0.001	0.002	0.167	0.001	0.001
Ba	0.093	0.087	0.014	0.079	0.080	0.079	0.069	0.075	0.086	0.079	0.094	0.010	0.101	0.086
Total	15.665	15.661	14.062	15.693	15.715	15.671	15.693	15.564	15.549	15.691	15.585	13.983	15.711	15.675
Mg#	0.903	0.898	0.751	0.888	0.890	0.884	0.908	0.918	0.908	0.936	0.927	0.755	0.932	0.935

Mg# = Mg/(Mg+Fe), Pg- paragonite, Phl-phlogopite.

hydrothermal zircons from P-type jadeitite and eclogite veins (e.g., Glodny et al., 2008; Meng et al., 2011; Rubatto, 2017; Rubatto and Hermann, 2003; Yui et al., 2010, 2012). These zircons are considered to have crystallized in metamorphic fluids rather than in melt (e.g., Glodny et al., 2008; Yui et al., 2010). In addition, the chromitite in dunite has yielded a Re—Os isotopic age of 470 Ma (Walker et al., 2002), which

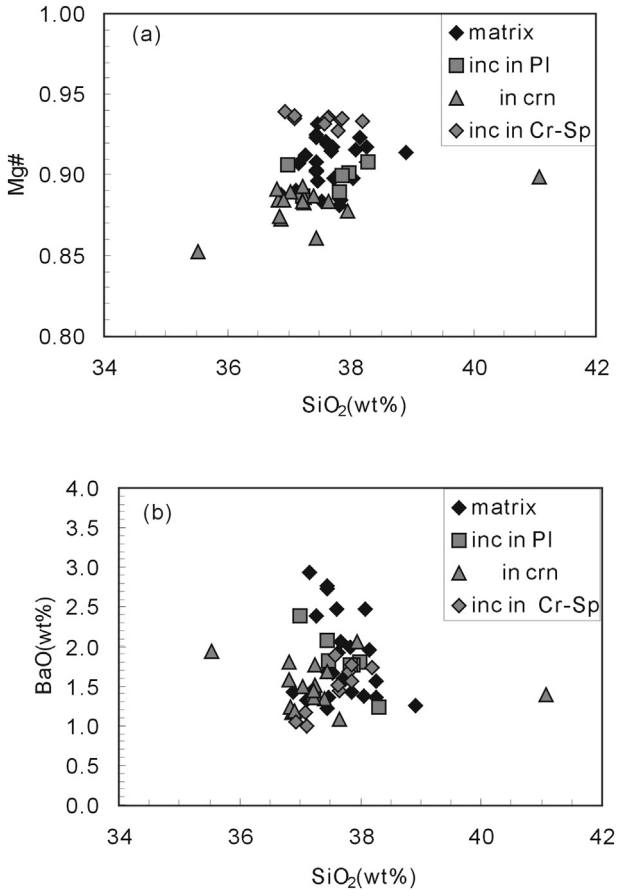

Fig. 7. Plots of Mg# vs. SiO_2 (wt%) variation of phlogopite (a) and Plots of BaO (wt%) vs. SiO_2 (wt%) variation of phlogopite (b). inc.-inclusions, Mineral abbreviations as Fig. 2.

implies the vein is 90 Myr younger than the country rocks. That long time gap between the formation of the vein and the country rocks indicates that the vein and dunite were not formed during a same magmatic event. Bryanchaninova et al. (2004) concluded that the vein was formed from the fractional crystallization of ultramafic magma. If it precipitated from ultramafic melt, then the vein and ultramafic rocks should have approximately the same age. However, the vein is ~40 Myr younger than the gabbro–diorite (zircon U—Pb age of 418 ± 2 Ma) that is present near the southeastern margin of the Rai–Iz ultramafic rocks (Shmelev and Meng, 2013). Thus, the red-corundum-bearing vein was not the product of this magmatic episode. Due to lack of contemporaneous magmatic activity, the formation mechanism of the red-corundum-bearing vein is analogous to the jadeitite veins in the Syum–Keu peridotite, which were the product of fluid influx into peridotite (Meng et al., 2011). Three localities of jadeitite mineralization (Obraztsov, Karovoe, and Zapadnoe) are exposed along the northeastern margin of the Rai–Iz Block (Kazak et al., 1976). Moreover, formation of platinum-group minerals in chromite implies that fluid intensely affected the Rai–Iz peridotite (Garuti et al., 1999). The fluid is considered to have been derived from the subducted slab (Bebout, 2007; Hermann et al., 2006; Manning, 2004; Peacock, 1990; Scambelluri et al., 2001; Spandler et al., 2011; Spandler and Pirard, 2013). The negative εHf(t) values of some zircons (−11 to −8) indicate input of ancient crustal material to the fluid. We infer that this material was derived from sediments of the subducted slab. The zircons also have a wide range of positive εHf (t) values (0 to +13; Fig. 10), implying that the fluid was derived from subducted oceanic crust and experienced varying degrees of contamination by ancient crustal material (Xu et al., 2007).

Oligoclase occurs mainly in the central and mica zones of the vein (Fig. 2a). The oligoclase An number and Al_2O_3 content decrease from core to rim of the crystals (Table 3) in these zones, which may be caused by corundum crystallization due to the following reaction: oligoclase (core, An_{28}) → oligoclase (rim, An_{25}) + corundum. Our results indicate that the vein minerals were crystallized from fluid, and the formation of corundum is attributed to desilication of the Na–Al–Si fluid rather than derivation from precursory pegmatite (Ishimaru et al., 2015; Simonet et al., 2008). Fluids from the downgoing slab supply Na, Al, and Si, which are the dominant solutes in subduction zone fluids (Manning, 2004; Spandler and Pirard, 2013). Red corundum in the samples contains a maximum Cr_2O_3 content of ~6.9 wt% (Table 1), Corundum with higher Cr_2O_3 content usually formed in deep mantle, such as the corundum inclusions in diamonds (8.6–19.3 wt%; Watt et al., 1994; Hutchison et al., 2004; Shi et al., 2011). Therefore, we infer that the red corundum precipitated in the shallow mantle, such as the mantle wedge above a subduecting slab. Cr derived from chromian spinel is transported by fluids, this is demonstrated by some high Cr_2O_3 minerals in ultramafic rocks. For example, chrome-rich clinopyroxene (Liu et al., 1998), Uvarovite in podiform chromitite (Proenza et al., 1999), kosmochlor-bearing diopside (Ikehata and Arai, 2004), Kosmochlor and chromian jadeite (Shi et al., 2005), hydrothermal chromite (Arai and Akizawa, 2014).

$\delta^{18}O$ value for the red corundum is 4.9‰ (Yakovenko et al., 2014). This $\delta^{18}O$ value is similar to those of hydrothermal corundum from Zimbabwe (3.5‰–4.8‰; Kerrich et al., 1987), mantle olivine (4.8‰–5.5‰) and spinel (4.37‰ ± 0.66) (Mattey et al., 1994), indicating that it crystallized in hydrothermal conditions and formed from fluid that reacted with chromian spinel or chromite.

Chromian spinel gradually increases in abundance from the mica zone to the wall-rock margins, indicating that it is closely related to the dunite (Ishimaru et al., 2015). The coarse chromian spinel is xenocrystic and derived from the wall rock dunite and/or chromitite (Ishimaru et al., 2015), which are enriched in Cr and Fe in the core and Al in the rim, respectively (Fig. 7). The coarse xenocrystic chromian spinel was possibly reworked by Al-enriched fluid, whereas the fine chromian spinel was precipitated under hydrothermal conditions (Fig. 6, grain 5).

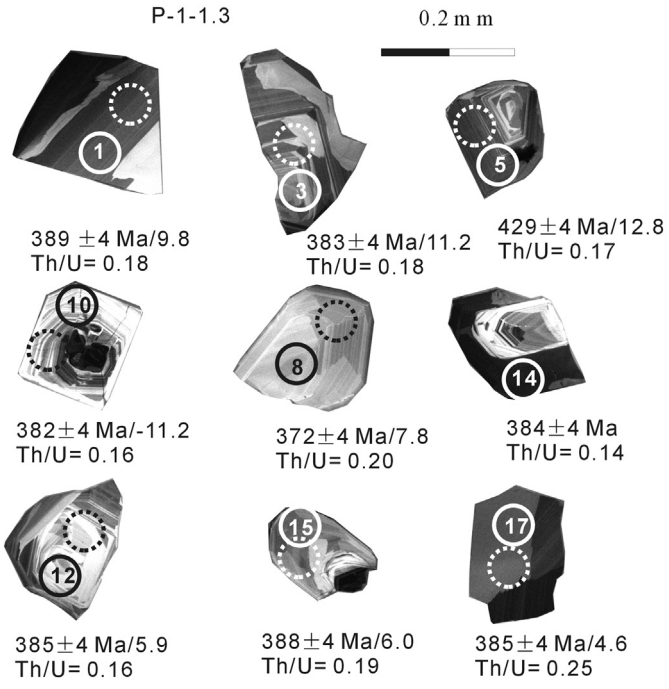

Fig. 8. Cathodoluminescence (CL) images of representative zircons from oligoclasite (P-1-1.3). The solid line circles-analytical spots of U-Pb; the dashed line circles-analytical spots of Lu—Hf. Undered the CL images are labeled values of $^{206}Pb/^{238}U$ ages (1σ error), εHf(t) and Th/U ratio.

Table 5
LA-MC-ICP MS U—Pb dating of zircon from the oligoclasite (P-1-1.3) of red-corundum-bearing vein in the Rai-Iz ultramafic rocks, Polar Urals, Russia.

Spots	Abundance			Isotopic ratios							Ages(Ma)					
	Pb(ppm)	*Th(ppm)*	U(ppm)	$^{232}Th/^{238}U$	$^{206}Pb/^{238}U$	1σ	$^{207}Pb/^{235}U$	1σ	$^{207}Pb/^{206}Pb$	1σ	$^{206}Pb/^{238}U$	1σ	$^{207}Pb/^{235}U$	1σ	$^{207}Pb/^{206}Pb$	1σ
1	13	37	213	0.18	0.0622	0.0006	0.4824	0.0083	0.0562	0.0008	389	4	400	7	462	32
2	29	60	501	0.12	0.0609	0.0006	0.4562	0.0069	0.0543	0.0007	381	4	382	6	385	29
3	8	24	143	0.18	0.0612	0.0006	0.4840	0.0077	0.0574	0.0008	383	4	401	6	505	31
4	4	6	70	0.09	0.0607	0.0007	0.4711	0.0130	0.0563	0.0013	380	4	392	11	464	51
5	5	13	78	0.17	0.0688	0.0007	0.7133	0.0139	0.0752	0.0013	429	4	547	11	1074	35
6	14	41	239	0.17	0.0598	0.0006	0.4474	0.0069	0.0543	0.0007	374	4	375	6	382	29
7	9	23	155	0.16	0.0599	0.0006	0.4576	0.0076	0.0554	0.0008	375	4	383	6	429	32
8	4	15	78	0.20	0.0594	0.0006	0.4563	0.0086	0.0557	0.0009	372	4	382	7	441	36
9	16	44	266	0.17	0.0614	0.0006	0.4636	0.0072	0.0548	0.0007	384	4	387	6	402	29
10	5	13	80	0.16	0.0611	0.0006	0.4624	0.0106	0.0549	0.0011	382	4	386	9	408	45
11	6	22	112	0.20	0.0599	0.0006	0.4543	0.0078	0.0550	0.0008	375	4	380	7	412	33
12	4	12	74	0.16	0.0616	0.0007	0.4622	0.0097	0.0544	0.0010	385	4	386	8	388	41
13	10	37	168	0.22	0.0613	0.0006	0.4681	0.0075	0.0554	0.0007	384	4	390	6	428	28
14	25	58	432	0.14	0.0614	0.0006	0.4720	0.0070	0.0558	0.0007	384	4	393	6	443	28
15	6	19	103	0.19	0.0621	0.0006	0.4608	0.0081	0.0538	0.0008	388	4	385	7	363	34
16	17	48	290	0.17	0.0617	0.0006	0.4649	0.0071	0.0546	0.0007	386	4	388	6	398	29
17	9	38	158	0.25	0.0615	0.0006	0.4572	0.0073	0.0539	0.0007	385	4	382	6	368	29
18	9	31	144	0.22	0.0617	0.0006	0.4618	0.0073	0.0543	0.0007	386	4	386	6	383	29
19	9	11	140	0.08	0.0613	0.0007	0.4726	0.0118	0.0559	0.0011	384	4	393	10	449	44
20	6	7	102	0.07	0.0622	0.0007	0.4683	0.0083	0.0546	0.0008	389	4	390	7	396	33

Analyses performed at the Isotopic Laboratory, Tianjin Institute of Geology and Mineral Resources.

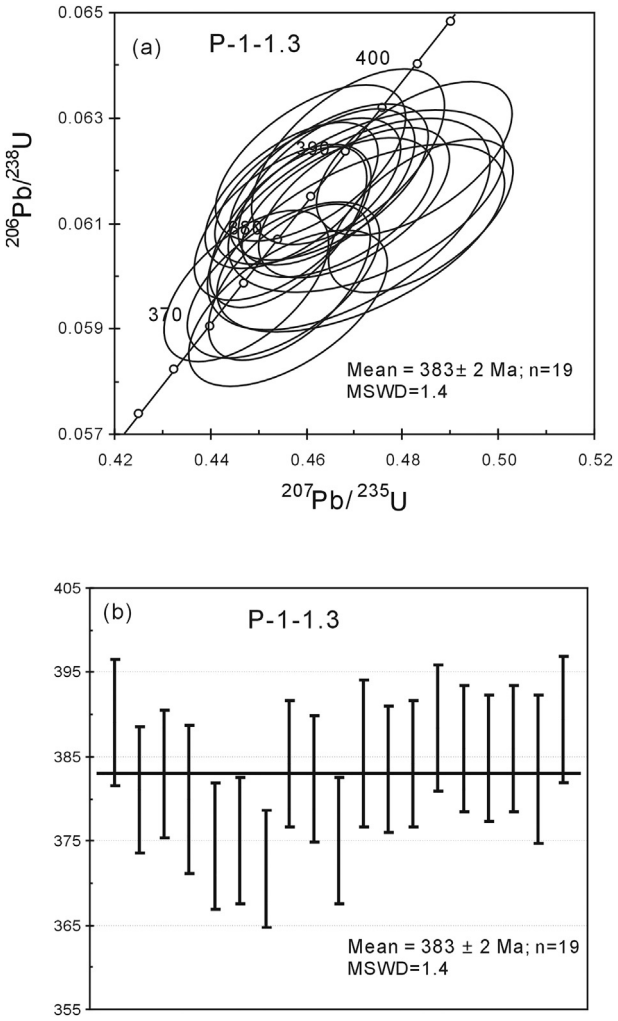

Fig. 9. (a) Concordia ages diagram by LA-MC-ICPMS analyses of the zircons from oligoclasite (P-1-1.3), error ellipses are 2σ. (b) Weighted mean ages of the $^{206}Pb/^{238}U$ ages for zircons.

The mica minerals are characterized by a wide range in BaO contents (1.2–24.6 wt%), which is indicative of different origins (Harlow, 1995). Phlogopite crystals in the studied samples have BaO contents of 1–3 wt% (Fig. 7), lower than those of the Guli peridotite massif in the Siberia, Russia (11 wt%; Kogarko et al., 2012) and higher than those of the Finero phlogopite peridotite in the Italian Alps (0.2–0.5 wt%; Exley et al., 1982) and the Kovdor phlogopite mine (<0.3 wt%; Krasnova, 2001) on the Kola Peninsula, Russia. Kogarko et al. (2012) concluded that phlogopite in the Guli peridotite massif was formed from BaO-rich primary magma. Ba-phengite from Guatemala jadeitite contains 0.4–4 wt% BaO and phlogopite contains 0.2–1.1 wt% BaO (Harlow, 1995). Jadeitite from Japan contains Ba-rich feldspar (Morishita, 2005). Ba-silicate minerals are found in the jadeitite from Myanmar (Shi et al., 2010). The Ba content of these minerals was derived from subduction zone metasediment (Harlow, 1995; Morishita, 2005; Shi et al., 2010). The Rai–Iz Massif was associated with a suprasubduction zone (Shmelev, 2011), and therefore the Ba content of the phlogopite was most likely derived from subducted oceanic sediment.

Paragonite commonly surrounds phlogopite in the studied samples. In contrast with the phlogopite (which is rich in Mg, K, and Ba), the paragonite is enriched in Na_2O (5.8–6.4 wt%) and SrO (1–2 wt%) (Table 4), indicating fluid evolution from K_2O + BaO to Na_2O + SrO. Eclogite from the Su–Lu ultrahigh-pressure belt in China contains Sr-rich zoisite and epidote (Nagasaki and Enami, 1998). Sr-rich epidote was also found in the Kurosegawa Zone in central Kyushu, Japan (Miyazoe et al., 2012). These Sr-bearing minerals were produced by breakdown of Sr-rich minerals in the subducted slab (Miyazoe et al., 2012; Nagasaki and Enami, 1998). In addition, Sr from seawater is readily incorporated into serpentinite during the serpentinization of peridotite (Scambelluri et al., 2001). Serpentine may be enriched in mobile elements such as As, Sb, B, Li, Cs, Pb, U, Ba, and Sr, and can transport these elements into the deep mantle before breakdown (Spandler and Pirard, 2013). Serpentinite releases Sr into the fluid during dehydration in a subduction zone.

6.3. Model of vein formation

Based on petrography, mineral chemistry, and geochemistry (Goldny et al., 2003; Bryanchaninova et al., 2004; Ishimaru et al., 2015; this study), the genesis of the red-corundum-bearing vein in the

Table 6
Lu—Hf isotopes of zircons from oligoclasite (P-1-1.3) of red-corundum-bearing vein in the Rai-Iz ultramafic rocks, Polar Urals, Russia.

Spots	Age/Ma	$^{176}Yb/^{177}Hf$	2σ	$^{176}Lu/^{177}Hf$	2σ	$^{176}Hf/^{177}Hf$	2σ	f(Lu/Hf)	εHf(0)	εHf(t)
1	389	0.004200	0.000009	0.000230	0.000000	0.282809	0.000025	-0.99	1.3	9.8
2	381	0.005150	0.000005	0.000333	0.000000	0.282785	0.000026	-0.99	0.5	8.7
3	383	0.002416	0.000023	0.000141	0.000001	0.282851	0.000032	-1.00	2.8	11.2
4	380	0.023539	0.000197	0.001197	0.000010	0.282295	0.000028	-0.96	-16.9	-8.8
5	429	0.003322	0.000030	0.000191	0.000002	0.282863	0.000030	-0.99	3.2	12.6
6	374	0.002593	0.000030	0.000151	0.000002	0.282787	0.000030	-1.00	0.5	8.7
8	372	0.000853	0.000009	0.000046	0.000000	0.282763	0.000030	-1.00	-0.3	7.8
9	384	0.002778	0.000013	0.000164	0.000001	0.282762	0.000032	-1.00	-0.3	8.0
10	382	0.016136	0.000060	0.000760	0.000003	0.282225	0.000034	-0.98	-19.4	-11.2
11	375	0.001233	0.000010	0.000067	0.000000	0.282798	0.000032	-1.00	0.9	9.1
12	385	0.001705	0.000032	0.000096	0.000002	0.282701	0.000031	-1.00	-2.5	5.9
13	384	0.004710	0.000009	0.000255	0.000000	0.282577	0.000033	-0.99	-6.9	1.5
14	388	0.001694	0.000031	0.000093	0.000002	0.282701	0.000031	-1.00	-2.5	6.0
15	386	0.002730	0.000010	0.000159	0.000001	0.282544	0.000023	-1.00	-8.1	0.4
16	385	0.000689	0.000010	0.000036	0.000000	0.282665	0.000027	-1.00	-3.8	4.6
18	386	0.003947	0.000022	0.000227	0.000001	0.282855	0.000030	-0.99	3.0	11.4
19	384	0.002998	0.000053	0.000171	0.000003	0.282618	0.000031	-0.99	-5.4	2.9
20	389	0.001305	0.000011	0.000071	0.000000	0.282640	0.000027	-1.00	-4.7	3.9
22	380	0.013165	0.000229	0.000644	0.000012	0.282281	0.000027	-0.98	-17.4	-9.2
23	380	0.001899	0.000018	0.000105	0.000001	0.282636	0.000027	-1.00	-4.8	3.5
25	380	0.000748	0.000010	0.000053	0.000000	0.282598	0.000030	-1.00	-6.2	2.2
26	380	0.000651	0.000039	0.000043	0.000002	0.282618	0.000032	-1.00	-5.4	2.9
27	380	0.003893	0.000158	0.000197	0.000008	0.282539	0.000033	-0.99	-8.2	0.0

Analyses performed at Institute of Mineral Resources,CAGS, Beijing

dunite of the Rai–Iz peridotite is related to metasomatism in the mantle wedge (Goldny et al., 2003; Ishimaru et al., 2015). According to the equilibrium of corundum with oligoclase and absence of jadeite in representative samples, this metasomatism occurred at conditions of 600 °C–700 °C and 1.0–1.5 GPa (Ishimaru et al., 2015) at about 380 Ma (Goldny et al., 2003; this study). The formation of jadeitite in the Rai–Iz peridotite (Kazak et al., 1976) was related to subduction of the oceanic slab (Meng et al., 2011). Furthermore, the metasomatic fluids that formed the red-corundum-bearing vein were derived from the subducted slab rather than from magmatic–hydrothermal fluids (Bryanchaninova et al., 2004).

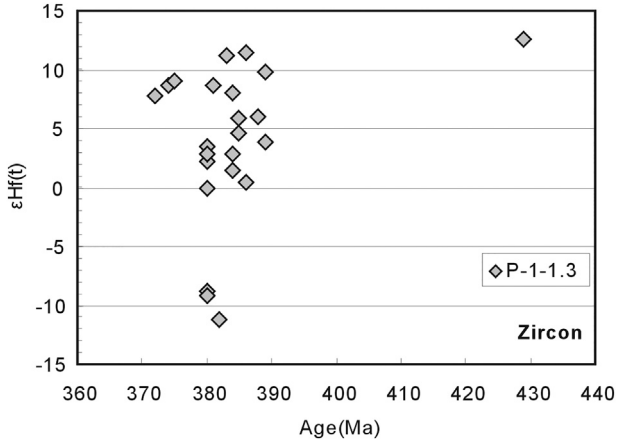

Fig. 10. Diagram of $^{206}Pb/^{238}U$ ages vs εHf(t) values of the zircons from oligoclasite (P-1-1.3).

7. Conclusions

1. Dating of zircon and phlogopite yielded ages of 380 Ma, which represent the age of the red-corundum-bearing vein.
2. On the basis of occurrence, mineral assemblages, mineral chemistry, and age, we conclude that the red-corundum-bearing vein was the product of fluid interaction with peridotite in a mantle wedge.
3. The subducted oceanic slab was the source of the fluid and vein material. The Cr content of the red corundum was potentially derived from accessory chromian spinel in the peridotite.
4. The genesis of the red-corundum-bearing vein was associated with subduction zone recycling, whereby crustal material circulated into the mantle wedge and reacted with peridotite to form metasomatic rocks containing red corundum.

Table 7
Isotopic data of $^{40}Ar/^{39}Ar$ step heating analysis of the phlogopite (PU-6) from red-corundum-bearing rock in the Rai-Iz ultramafic rocks, Polar Urals, Russia.

Sample	T(°C)	Age	±Age	$\%^{40}Ar^*$	^{39}Ar(Mols)	^{40}Ar	$\pm^{40}Ar$	^{39}Ar	$\pm^{39}Ar$	^{38}Ar	$\pm^{38}Ar$	^{37}Ar	$\pm^{37}Ar$	^{36}Ar	$\pm^{36}Ar$
J=0.005113															
PU-6	850	231.71	5.75	80.39	1.48E-14	30.87093	0.07683	0.92689	0.00182	0.08697	0.00151	1.62146	0.00080	0.02091	0.00226
PU-6	900	368.61	0.97	95.42	2.21E-14	64.29362	0.03554	1.38398	0.00165	0.04240	0.00265	0.48776	0.00217	0.01007	0.00060
PU-6	950	324.15	3.44	92.68	7.21E-15	18.73259	0.01962	0.45128	0.00186	0.02040	0.00590	0.45717	0.00385	0.00475	0.00067
PU-6	1000	349.55	2.61	93.78	1.07E-14	29.83180	0.02690	0.66920	0.00551	0.01872	0.00250	0.28125	0.00324	0.00634	0.00029
PU-6	1050	363.40	3.23	98.20	1.13E-14	31.53907	0.15576	0.71008	0.00347	0.02327	0.00025	0.68041	0.00190	0.00209	0.00104
PU-6	1100	377.64	1.72	95.63	2.70E-14	80.49506	0.15095	1.69044	0.00824	0.02245	0.00718	0.15472	0.00448	0.01190	0.00109
PU-6	1150	377.78	1.66	97.42	1.87E-14	54.86792	0.00619	1.17346	0.00064	0.02519	0.00331	0.31402	0.00156	0.00485	0.00088
PU-6	1200	377.38	2.28	97.39	1.71E-14	49.87905	0.03761	1.06779	0.00426	0.02477	0.00333	0.38611	0.00219	0.00448	0.00097
PU-6	1250	373.40	4.47	98.48	1.31E-14	37.41250	0.00964	0.81946	0.00588	0.02275	0.00398	0.39761	0.00103	0.00202	0.00142
PU-6	1300	262.42	3.03	81.85	5.51E-15	12.89199	0.01210	0.34493	0.00342	0.02054	0.00194	0.51480	0.00196	0.00805	0.00029
PU-6	1400	112.68	6.40	61.53	3.36E-15	4.30454	0.00791	0.21053	0.00788	0.02811	0.00132	0.62943	0.00065	0.00577	0.00013

Analyses performed at Key Laboratory of Orogen and Crust Evolution, Peking University

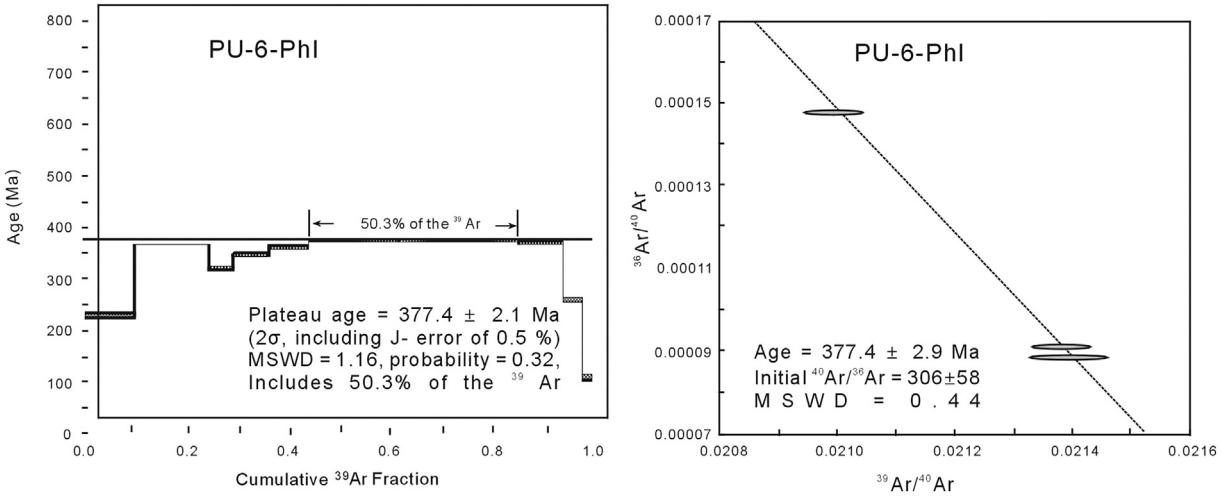

Fig. 11. $^{40}Ar/^{39}Ar$ plateau ages and isochron ages of phlogopite (sample PU-6).

This case reveals the veins in the mantle wedge peridotite are recorder of the fluid activity in subduction zone, it reflect material circulation between crust and mantle.

Acknowledgements

We thank Nikolay Yushkin for providing the red-corundum-bearing samples, and Vladimir Nuzhin, Ivan Popov, and Tianfu Li for assistance during fieldwork in the Polar Urals. He Rong (Institute of Geology, CAGS, China) provided assistance with EPMA. We greatly appreciate Editor-in-Chief Xian-Hua Li, reviewers Shoji Arai and Johannes Glodny for their constructive comments. The Key Laboratory of Orogen and Crust Evolution (Peking University, China) is thanked for assistance with the phlogopite data processing. This work was supported by the National Natural Science Foundation of China (41672031, 41072026) and Program the Russian Academy of Sciences (No.0393-2016-0020).

References

Andersen, T., 2002. Correction of common lead in U–Pb analyses that do not report ^{204}Pb. Chemical Geology 192, 59–79.
Arai, S., Akizawa, N., 2014. Precipitation and dissolution of chromite by hydrothermal solutions in the Oman ophiolite: New behavior of Cr and chromite. American Mineralogist 99, 28–34.
Bebout, G.E., 2007. Metamorphic chemical geodynamics of subduction zones. Earth and Planetary Science Letters 260, 373–393.
Bryanchaninova, N.I., Makeev, A.B., Zubkova, N.V., Filipov, N.V., 2004. Sodium-Strontium Mica $Na_{0.50}Sr_{0.25}Al_2(Na_{0.25}\square_{0.75})Al_{1.25}Si_{2.75}O_{10}(OH)_2$ from Rubinovyi Log. Doklady Earth Sciences 395, 260–265.
Chu, N.C., Taylor, R.N., Chavagnac, V., Nesbitt, R.W., Boella, R.M., Milton, J.A., German, C.R., Bayon, G., Burton, K., 2002. Hf isotope ratio analysis using multi-collector inductively coupled plasma mass spectrometry: an evaluation of isobaric interference corrections. Journal of Analytical Atomic Spectrometry 17, 1567–1574.
Elhlou, S., Belousova, E., Griffin, W.L., Pearson, N.J., O'Reilly, S.Y., 2006. Trace element and isotopic composition of GJ-red zircon standard by laser ablation (Suppl.). Geochimica et Cosmochimica Acta A158.
Exley, R.A., Sills, J.D., Smith, J.V., 1982. Geochemistry of mica from the Finero spinel-lherzolite, Italian Alps. Contrib. Mineral. Petrol. 81, 59–63.
Garuti, G., Zaccarini, F., Moloshag, V., Alimov, V., 1999. Platinum-group minerals as indications of sulfur fugacity in ophiolitic upper mantle: an example from chromitites of the Ray-Is ultramafic complex, Polar Urals, Russia. The Canadian Mineralogist 37, 1099–1115.
Glodny, J., Pease, V.L., Montero, P., Austrheim, H., Rusin, A.I., 2004. Protolith ages of eclogites, Marun-Keu complex, Polar Urals, Russia: implications for the pre- and early Uralian evolution of the northeastern European continenral margin. Geol. Soc. Lond. 30, 87–105.
Glodny, J., Kuhn, A., Austrheim, H., 2008. Geochronology of fluid-induced eclogite and amphibolite facies metamorphic reactions in a subduction–collision system, Bergen Arcs, Norway. Contributions to Mineralogy and Petrology 156, 27–48.
Goldny, J., Austrheim, H., Molina, J.F., Rusin, A., Seward, D., 2003. Rb/Sr record of fluid-rock interaction in eclogites: The Marun-Keu complex, Polar Urals, Russia. Geochimica et Cosmochimica Acta 67, 4353–4371.
Gong, J.F., Ji, J.Q., Sang, H.Q., Han, B.F., Li, B.L., Chen, J.J., 2006. $^{40}Ar/^{39}Ar$ geochronology of high-pressure granulite xenolith and its surrounding granite in central Himalaya. Acta Petrologica Sinica 22, 2677–2686 (in Chinese with English abstract).
Hadley, J.B., 1949. Preliminary report on corundum deposits in the Buck Creek peridotite Clay County, North Carolina. United States Geological Survey Bulletin 948E, 103–128.
Harley, S.L., Kelly, N.M., Moller, A., 2007. Zircon behaviour and the thermal histories of mountain chains. Elements 3, 25–30.
Harlow, G.E., 1995. Crystal chemistry of barian enrichment in micas from metasomatized inclusions in serpentinite, Motagua Fault Zone, Guatemala. European Journal of Mineralogy 7, 775–789.
Harlow, G.E., Sorensen, S.S., 2005. Jade (Nephrite and Jadeitite) and serpentinite: metasomatic connections. International Geology Review 47, 113–146.
Hattori, K.H., Guillot, S., Saumur, B.M., Tubrett, M.N., Vidal, O., Morfin, S., 2010. Corundum-bearing garnet peridotite from northern Dominican Republic: A metamorphic product of an arc cumulate in the Caribbean subduction zone. Lithos 114, 437–450.
Hermann, J., Spandler, C., Hack, A., Korsakov, A.V., 2006. Aqueous fluids and hydrous melts in high-pressure and ultra-high pressure rocks: Implications for element transfer in subduction zones. Lithos 92, 399–417.
Hou, K.J., Li, Y.H., Zou, T.R., Qu, X.M., Shi, Y.R., Xie, G.Q., 2007. Laser ablation-MC-ICP-MS technique for Hf isotope microanalysis of zircon and its geological applications. Acta Petrologica Sinica 23, 2595–2604 (in Chinese with English abstract).
Huang, D.Z., Gao, J., Dai, T.G., Zou, H.Y., Xiong, X.M., Klemd, R., 2005. Origin of the deep fluids in the paleosubduction zones in western Tianshan: Evidence from Pb- and Sr-isotope compositions of high-pressure veins and host rocks. Science China (Ser. D) 48, 1627–1636.
Hutchison, M.T., Nixon, P.H., Harley, S.L., 2004. Corundum inclusions in diamonds—discriminatory criteria and a corundum compositional dataset. Lithos 77, 273–286.
Iizuka, T., Hirata, T., 2005. Improvements of precision and accuracy in-situ Hf isotope microanalysis of zircon using the laser ablation-MC-ICPMS technique. Chemical Geology 220, 121–137.
Ikehata, K., Arai, S., 2004. Metasomatic formation of kosmochlor-bearing diopside in peridotite xenoliths from North Island, New Zealand. American Mineralogist 89, 1396–1404.
Ishimaru, S., Arai, S., Miura, M., Shmelev, V.R., Pushkalev, E., 2015. Ruby-bearing feldspathic dike in peridotite from Ray-Iz ophiolite, the Polar Urals: implications for the mantle metasomatims and origin of ruby. Journal of Mineralogical and Petrological Sciences 110, 76–81.
Kazak, A.P., Dobretsov, N.L., Moldavantsev, Yu.E., 1976. Glaucophane schists, jadeitites, vesuvianites and nephrites of ultrabasitic Rai-Iz massif. Geology and Geophysics (2), 60–66 (in Russian).
Kerrich, R., Fyfe, W.S., Barnett, R.L., Blair, B.B., Willmore, L.M., 1987. Corundum, Cr-muscovite rocks at O'Briens, Zimbabwe: the conjunction of hydrothermal desilicification and LIL-element enrichment- geochemical and isotopic evidence. Contributions to Mineralogy and Petrology 95, 481–497.
Kogarko, L.N., Ryabchikov, I.D., Kuzmin, D.V., 2012. High-Ba mica in olivinites of the Guli massif (Maimecha–Kotui province, Siberia). Russian Geology and Geophysics 53, 1209–1215.
Kolesnik, Yu.N., 1976. High temperature metasomatism in ultramafic massif. Novosibirsk: Nauka 1–238 (in Russian).
Krasnova, N.I., 2001. The Kovdor phlogopite deposite, Kola peninsula, Russia. The Canadian Mineralogist 39, 33–44.
Lawson, A.C., 1904. Plumasite, an oligoclase-corundum rock near Spanish Peak, California. University of California, Department of Geological Sciences Bulletin 3, 219–229.
Liu, X.C., Zhou, H.Y., Ma, Z.S., Chang, L.H., 1998. Chrome-rich clinopyroxene in orthopyroxenite from Maowu, Dabie Mountains, central China: a second record and its implications for petrogenesis. The Island Arc 7, 135–141.
Liu, Y.S., Gao, S., Hu, Z.C., Gao, C.G., Zong, K.Q., Wang, D.B., 2010. Continental and oceanic crust recycling-induced melt-peridotite interactions in the Transe North China

orogen: U-Pb dating, Hf isotopes and trace elements in zircons from mantle xenoliths. Journal of Petrology 51, 537–571.
Ludwig, K.R., 2003. User's Manual for Isoplot 3.00: A Geochronological Toolkit for Microsoft Excel. 4. Berkeley Geochronology Center Special Publication, Berkeley, USA, p. 70.
Makeyev, A.B., 2006. Typomorphic features of Cr-spinel and mineralogical prospecting guides for Cr ore mineralization. Russian Journal of Earth Sciences 8, ES3002. https://doi.org/10.2205/2006ES000196.
Makeyev, A.B., Perevozchikov, B.V., Afanacyev, A.K., 1985. Chromite in the Polar Urals. Komi Branch of the Academy of Sciences of USSR. Syktyvkar, Russia, pp. 1–152 (in Russian).
Manning, C.E., 2004. The chemistry of subduction-zone fluids. Earth and Planetary Science Letters 223, 1–16.
Mattey, D.P., Lowry, D., Macpherson, C.G., Chazot, G., 1994. Oxygen isotope composition of mantle minerals by laser fluorination analysis: homogeneity in peridotites, heterogeneity in eclogites. Goldschmidt Conference (Edinburgh) 573–574.
Meng, F.C., Makeyev, A.B., Yang, J.S., 2011. Zircon U-Pb dating of jadeitite from the Syum-Keu ultramafic complex, Polar Urals, Russia: Constraint for subduction initiation. Journal of Asian Earth Sciences 42, 596–606.
Miyazoe, T., Enami, M., Nishiyama, T., Mori, Y., 2012. Retrograde strontium metasomatism in serpentinite melange of the Kurosegawa Zone in central Kyushu, Japan. Mineralogical Magazine 76, 635–647.
Moldavantsev, Yu. E., Kazak, A. P., 1977. Rai-Iz massif. In: Sobolev, V. S., and Dobretsov, N. L., (Eds.), Petrology and metamorphism of ancient ophiolites (Polar Urals and West Sayan as examples). Nauka. Novosibirsk, 38–59 (in Russian).
Morishita, T., 2005. Occurrence and chemical composition of barian feldspars in a jadeitite from the Itoigawa-Omi District in the Renge high-P/T-type metamorphic belt, Japan. Mineralogical Magazine 69, 39–51.
Nagasaki, A., Enami, M., 1998. Sr-bearing zoisite and epidote in ultra high-pressure (UHP) metamorphic rocks from the Su-Lu province, eastern China: an important Sr-reservoir under UHP conditions. American Mineralogist 83, 240–247.
Nelson, B.K., 1991. Sediment-derived fluids in subduction zones: isotopic evidence from veins in blueschist and eclogite of the Franciscan Complex, California. Geology 19, 1033–1036.
Nelson, B.K., 1995. Fluid flow in subduction zones: evidence from Nd- and Sr-isotope variations in metabasalts of the Franciscan complex, California. Contributions to Mineralogy and Petrology 119, 247–262.
Okay, A.I., 1994. Sapphirine and Ti-clinohumite in ultra-high-pressure garnet-pyroxenite and eclogite from Dabie Shan, China. Contributions to Mineralogy and Petrology 116, 145–155.
Pasava, J., Knesl, I., Vymazalova, A., Vavrin, I., Gurskaya, L.I., Kolbantsev, L.R., 2011. Geochemistry and mineralogy of platinum-group elements (PGE) in chromites from Centralnoye I, Polar Urals, Russia. Geoscience Frontiers 2, 81–85.
Peacock, S.M., 1990. Fluid processes in subduction zones. Science 248, 329–337.
Perevozchikov, B.V., Chashchukhin, I.S., Tsritsyn, E.P., 1990. Metamorphism ultramafic rocks of massif and their primary compositions. In: Puchkov, V.N., Shteinberg, D.S. (Eds.), Structure, Evolution and Metallogeny of the Rai-Iz Ultramafic Massif. Sverdlovsk: The Ural Branch of the Academy of Sciences of SSSR, pp. 29–57 (in Russian).
Perevozchikov, B.V., Kenig, V.V., Lukin, A.A., Ovechkin, A.M., 2005. Chromites of the Rai-Iz Massif in the Polar Urals (Russia). Geology of Ore Deposits 47, 203–248 (in Russian).
Pratt, J.H., 1906. Corundum and its occurrence and distribution in the United States. United States Geol. Surv. Bull. 1–168.
Proenza, J., Solé, J., Melgarejo, J.C., 1999. Uvarovite in podiform chromitite: The Moa-Baracoa ophiolitic massif, Cuba. Canadian Mineralogist 37, 679–690.
Ronkin, Yu.L., Priamonocov, A.P., Telegina, T.V., Lepehina, O.P., 2000. Dunite-harzburgite, dunite-wehrlite-clinopyroxenite-gabbro complex of Polar Urals: REE, Sr-Nd constraints. Isotopic dating of geological process: new methods and results. Abstract of report I Russian conference on isotopic geochronology. Moscow, pp. 302–305 (in Russian).
Rubatto, D., 2017. Zircon: the metamorphic mineral. Reviews in Mineralogy and Geochemistry 83, 261–295.
Rubatto, D., Hermann, J., 2003. Zircon formation during fluid circulation in eclogites (Monviso, Western Alps): implications for Zr and Hf budget in subduction zones. Geochimica et Cosmochimica Acta 67, 2173–2187.
Scambelluri, M., Rampone, E., Piccardo, G.B., 2001. Fluid and element cycling in subducted serpentinite: A trace element study of the Erro-Tobbio high-pressure ultramafites (Western Alps, NW Italy). Journal of Petrology 42, 55–67.
Shi, G.H., Stockhert, B., Cui, W.Y., 2005. Kosmochlor and chromian jadeite aggregates from Myanmar area. Mineralogical Magazine 69, 1059–1075.
Shi, G.H., Jiang, N., Wang, Y.W., Zhao, X., Wang, X., Li, G.W., Ng, E., Cui, W.Y., 2010. Ba minerals in clinopyroxene rocks from the Myanmar jadeitite area: implications for Ba recycling in subduction zones. European Journal of Mineralogy 22, 199–214.
Shi, N.C., Lu, Q., Li, G.W., Liu, H.F., 2011. A species of high pressure mineral: the high-chromium corundum (ruby) as an inclusion in diamond from the Yuanshui, Hunan, China. Earth Science Frontiers 18, 341–346 (in Chinese with English abstract).
Shmelev, V.R., 2011. Mantle ultrabasites of ophiolite complexes in the Polar Urals: petrogenesis and geodynamic environments. Petrology 19, 618–640.
Shmelev, V.R., Meng, F.C., 2013. Nature and Age of mafic rocks from ophiolite massif Rai-Iz (Polar Ural). Doklady Earth Sciences 451, 758–761.
Simonet, C., Fritsch, E., Lasnier, B., 2008. A classification of gem corundum deposits aimed towards gem exploration. Ore Geology Reviews 34, 127–133.
Solesbury, F.W., 1967. Gem corundum pegmatites in NE Tanganyika. Economic Geology 62, 983–991.
Spandler, C., Pirard, C., 2013. Element recycling from subducting slabs to arc crust: A review. Lithos 170-171, 208–223.
Spandler, C., Pettke, T., Rubatto, D., 2011. Internal and external fluid sources for eclogite-facies veins in the Monviso meta-ophiolite, Western Alps: Implications for fluid flow in subduction zones. Journal of Petrology 52, 1207–1236.
Udoratina, O.V., Kuznetsov, N.B., Larionov, A.N., Shishkin, M.A., 2008. U-Pb dating of plagiogranites from the Sobsky complex (Polar Urals). Collections "Petrology and Mineralogy of the northern Urals and Timan". Syktyvkar 5, 52–62.
Vakhrusheva, N.V., Ivanov, K.S., Stepanov, A.E., Shokalsky, S.P., Azanov, A.N., Hiller, V.V., Shiryayev, P.B., 2016. Plagioclasites from chromite-bearing ultramafic rocks of the Rai-Iz massif. Lithosphere (Russia) 134–145, 16 (in Russian with English abstract).
Walker, R.J., Prichard, H.M., Ishiwatari, A., Pimentel, M., 2002. The osmium isotopic composition of convecting upper mantle deduced from ophiolite chromites. Geochimica et Cosmochimica Acta 66, 329–345.
Watt, G.R., Harris, J.W., Harte, B., Boyd, S.R., 1994. A high-chromium corundum (ruby) inclusion in diamond from the Sao Luiz alluvial mine, Brazil. Mineralogical Magazine 58, 490–492.
Wu, F.Y., Yang, Y.H., Xie, L.W., Yang, J.H., Xu, P., 2006. Hf isotopic compositions of the standard zircons and baddeleyites used in U-Pb geochronology. Chemical Geology 234, 105–126.
Xu, Y.G., Wu, X.Y., Luo, Z.Y., Ma, J.L., Huang, X.L., Xie, L.W., 2007. Zircon Hf isotope compositions of Middle Jurassic-Early Cretaceous intrusions in Shandong Provinece and its implications. Acta Petrologica Sinica 23 (2), 307–316.
Yakovenko, V.V., Vysotskiy, S.V., Karabtsov, A.A., 2014. Features of the oxygen isotopic composition of corundum bearing pegmatites and metasomatites in the Urals and Baikal. Lithosphere (Russia) 3, 140–144 (in Russian).
Yui, T.-F., Maki, K., Usuki, T., Lan, C.-Y., Martens, U., Wu, C.-M., Wu, T.-W., Liu, J.-G., 2010. Genesis of Guatemala jadeitite and related fluid characteristics: insight from zircon. Chemical Geology 270, 45–55.
Yui, T.F., Maki, K., Wang, K.L., Lan, C.Y., Usuki, T., Iizuka, Y., Wu, C.M., Wu, T.W., Nishiyama, T., Martens, U., Liou, J.G., Grove, M., 2012. Hf isotope and REE compositions of zircon from jadeitite (Tone, Japan and north of the Motagua fault, Guatemala): implications on jadeitite genesis and possible protoliths. European Journal of Mineralogy 24, 263–275.
Zhang, R.Y., Liou, J.G., Zheng, J.P., 2004. Ultrahigh-pressure corundum-rich garnetite in garnet peridotite, Sulu terrane, China. Contributions to Mineralogy and Petrology 147, 21–31.